Surface and Subsurface Dipole Variability in the Indian Ocean and Its Relation with ENSO

Toshiaki Shinoda

NOAA-CIRES Climate Diagnostics Center
325 Broadway
Boulder, CO 80305
toshiaki.shinoda@cdc.noaa.gov
Fax: 303-497-6449
Tel: 303-497-4295

Harry H. Hendon

Bureau of Meteorology Research Centre
PO Box 1289K, Melbourne 3001, AUSTRALIA

Michael A. Alexander

NOAA-CIRES Climate Diagnostics Center
325 Broadway
Boulder, CO 80305

revised

August 9, 2003

Abstract

An ocean general circulation model, forced with observed winds for the period 1958-97, is used to examine surface and subsurface temperature variability in the Indian Ocean and its relation to ENSO. Empirical orthogonal function (EOF) analysis of temperature anomalies in the equatorial longitude-depth plane indicates that the leading mode of variability has a dipole character, with strongest loadings in the thermocline and more modest loadings at the surface. The subsurface dipole is weakly correlated with Nino3.4 SST. However, the subsurface dipole is well correlated with dipole variability at the surface, which itself is well correlated with ENSO. These results indicate that "dipole" variability that is independent of ENSO is more prominent at depth than in the SST. While the influence of ENSO on subsurface variability is detectable, the ENSO-induced surface dipole is primarily controlled by surface heat fluxes. On the other hand, subsurface variations play an important role for surface dipole events that are independent of ENSO. This is especially true in the eastern Indian Ocean where the strong surface cooling in late summer is generated by upwelling and horizontal heat advection in response to basin-wide surface easterlies.

Keywords

Upper ocean process

Indian Ocean

1. Introduction

The structure of the leading mode of interannual variation of sea surface temperature (SST) in the tropical Indian Ocean varies with season. During boreal winter and spring the leading mode is same-signed throughout the basin, while during late boreal summer and autumn it has a zonal dipole structure (e.g., Saji et al. 1999; Baquero-Bernal et al. 2002; Shinoda et al. 2003). The basin-scale mode is thought to result from the lagged response to mature ENSO conditions in the Pacific (e.g., Klein et al. 1999). The origins of the dipole mode are controversial.

The dipole mode is readily identified by empirical orthogonal function (EOF) analysis of seasonal mean SST (e.g., Shinoda et al. 2003). Figure 1a shows the leading EOF of September-October-November (SON) mean SST based on the Reynolds and Smith (1994) weekly analyses for the period 1982-1999. Similar to the leading mode computed by Shinoda et al. (2003) based on the Smith et al. (1996) reconstructed SST for the period 1950-1999, the leading EOF has strongest loadings near and to the south of the equator in the eastern portion of the basin, with oppositely signed, but weaker, loadings covering most of the western portion of the basin. While a semantical debate exists as to whether this zonally out-of-phase behavior warrants being described as a dipole (Hastenrath 2002), its occurrence is intimately tied to zonal wind anomalies in the central Indian Ocean and rainfall anomalies in eastern Africa and Indonesia (e.g., Flohn 1986; Hastenrath et al. 1993; Saji et al. 1999; Hendon 2003).

Besides the debate about whether this zonally out-of-phase behavior is appropriately described as a dipole mode, there is an ongoing argument as to whether this dipole variability arises from coupled behavior inherent to the Indian Ocean (e.g., Saji et al. 1999; Webster et al. 1999) or whether it is mainly driven by ENSO variability

in the tropical Pacific (e.g., Baquero-Bernal et al. 2002; Shinoda et al. 2003). The strong correlation (0.74) of the dipole SST mode with the Nino3.4 SST index (Fig. 1b) provides persuasive evidence that ENSO is largely responsible for its occurrence. (Note that the correlation varies in the SST data set and period analyzed, e.g., Rao et al. 2002). In the paradigm of the atmospheric bridge (e.g., Alexander et al. 2002; Lau and Nath 2003; Shinoda et al. 2003), ENSO affects the Indian Ocean because the Walker circulation shifts eastward towards the date line (e.g., Rassmusson and Carpenter 1982, Latif and Barnett 1995), resulting in anomalous easterlies and suppressed rainfall over Indonesia and the eastern Indian Ocean. The easterly anomalies during late summer and autumn enhance the mean easterly winds in the Indonesian region, resulting in anomalous evaporative cooling in the eastern Indian Ocean. The easterlies also promote coastal upwelling off of Sumatra and Java (e.g., Vinayachandran et al. 2002) and generate westward propagating Rossby waves, which suppress the thermocline and promote surface warming (together with enhanced insolation) to the west (e.g., Chambers et al. 1999; Murtugudde and Busalacchi 1999, Murtugudde et al. 2000, Xie et al. 2001). Once the Australian monsoon onsets in December, the same easterly anomalies then act to reduce the wind speed in the eastern Indian Ocean. Thus, SSTs warm rapidly in the eastern Indian Ocean beginning in December, thereby yielding a basin-scale warm anomaly by boreal spring (e.g. Klein et al. 1999, Venzke et al. 2000). The relative roles of subsurface ocean dynamics and surface heat flux forcing for driving the SST variation during the ENSO cycle is still unclear. However, surface heat flux forcing alone produces SST variations during ENSO that are phase-locked to the seasonal cycle in a qualitatively correct fashion (e.g., Hendon 2003, Shinoda et al. 2003).

On the other hand, a number of strong dipole events have developed in the absence of well defined ENSO variations in the Pacific (e.g., in 1961; Flohn 1986;

Reverdin et al. 1986; Saji et al 1999), thus supporting the notion that ENSO maybe not a necessary stimulus. Furthermore, subsurface dipole variability, which is more prominent than at the surface, is less correlated with ENSO than is the surface dipole (e.g., Rao e al. 2002).

In an attempt to reconcile some of these conflicting results, we examine dipole variability in the Indian Ocean at the surface and subsurface from a 40-year integration of an OGCM forced with observed surface fluxes. We focus on the differences in the surface and subsurface evolution during ENSO and during development of subsurface dipole events. The upper ocean heat budget is calculated in order to understand the dominant processes that control SST variations in each case.

This paper is organized as follows: The model, observed surface flux forcing and comparison of the model temperature with observations are described in section 2. Section 3 discusses the subsurface dipole variation, its relation to ENSO and its relation to surface forcings. In section 4, composites based on EOF analysis of subsurface temperatures and based on ENSO events are developed. The upper ocean heat budget is computed in order to identify the contrasting processes that control the SST evolution. Finally, discussion and conclusions are provided in Section 5.

2. Model Experiments

We employ output from a 40-year simulation of the National Center for Atmospheric Research ocean model (NCOM), which is based on the Geophysical Fluid Dynamics Laboratory (GFDL) Modular Ocean Model. The model is global with horizontal resolution of 2.4° in longitude. Meridional grid spacing smoothly increases from about 0.6° near the equator to about 1.2° at high latitude. Vertical mixing is based on the K-profile parameterization (KPP) of the upper ocean boundary layer (Large et al. 1994). Horizontal mixing is based on the mesoscale eddy parameterization described by Gent and McWilliams (1990). An anisotropic horizontal viscosity parameterization (Large et al. 2001) with enhanced viscosity close to boundaries and much weaker viscosity in the interior is also included. A detailed description of the model physics is found in Large et al. (1997), Gent et al. (1998) and Large et al. (2001).

The model is forced with surface fluxes of momentum, heat and freshwater for the period 1958-97. The wind stress is computed from the reanalysis fields produced at the National Center for Environmental Prediction (NCEP; Kalnay et al. 1996) using standard bulk formulae (Large and Pond 1982). The sensible and latent heat fluxes are estimated from NCEP surface winds, humidity, air temperature at 2m and model SST using standard air-sea transfer formula (Large and Pond 1982).

Net shorwave radiation at the surface based on cloud data from ISCCP (Bishop and Rossow 1991, Rossow and Schiffer 1991) is used when the data are available (1984-91). The ISCCP monthly climatology is used prior to 1984 and after 1991. Shortwave radiation is allowed to penetrate below the model surface using the two band approximation of Paulson and Simpson (1977). Monthly precipitation is obtained by combining MSU data (Spencer 1993) and estimates by Xie and Arkin (1996) from 1979 to 1993, while monthly climatologies of the two datasets are used

prior to 1979.

The model was integrated from the initial condition obtained from a preliminary climatological integration. The model was then run for two 40 years cycle, with the second cycle continuing from the end of the first cycle. The monthly output for the second 40-yr period integration is analyzed here. Further details of the model configuration are found at http://www.cgd.ucar.edu/oce/yeager/40.html.

In order to demonstrate that the model reasonably simulates observed variability in the Indian Ocean, SST and 20°C isotherm depth (D20) variation (proxy for thermocline variation) in the tropical western Indian Ocean (50°E-70°E, 10°S-10°N) and eastern Indian Ocean (90°E-110°E, 10°S-0) are compared with observations. These boxes are the same as those used by Saji et al. (1999) for their investigation of surface dipole variability. Monthly mean SST anomalies from the model are compared to observed monthly mean anomalies based on the weekly analyses of Reynolds and Smith (1996) for the period 1982-97 (Fig. 2a). Interannual variations are faithfully reproduced in the model. In particular, the large cooling events in the eastern Indian Ocean during 1994 and 1997 and warming events in 1983 and 1996 are well depicted.

Thermocline variations (D20 anomalies) from the model are compared to analyses produced at the Joint Environmental Data Analysis (JEDA) Center (White et al. 1998; Fig. 2b). While the correspondence between model and observed is not as great as at the surface, much of the interannual variability is captured by the model (the correlation coefficient between model and observed is 0.70 for the eastern box and 0.62 for the western box). For instance, the anomalous shallowing of the thermocline during 1994 and its recovery in 1995 in the eastern Indian Ocean is well represented in the model. It should be noted that the data coverage of the subsurface temperature in the tropical Indian Ocean is not as good as SST, and thus there is significant uncertainty of the observed D20 values. Overall, the model does a reasonable job

of reproducing the observed interannual variability and we proceed to diagnose its nature and causes.

3. Subsurface and surface dipole

The dominant mode of interannual variability of upper ocean heat content and sea level in the near equatorial Indian Ocean has zonal dipole structure with greatest amplitude in boreal autumn (e.g., Chambers et al. 1999; Rao et al. 2002). The strongest loadings are within 10 degrees of the equator and are displaced slightly south of the equator. This subsurface dipole variability is efficiently identified by EOF analysis of equatorially averaged temperature (5°N-10°S) in the longitude-depth plane. The leading EOF for boreal fall (SON) explains 72.3% of the variance in the longitude-depth plane (Fig. 3a). The strongest loadings are in the vicinity of the thermocline, with more modest loadings at the surface. The largest amplitude is in the eastern part of the ocean around 100°E-105°E. We will refer to this leading EOF as the subsurface dipole mode. The leading EOF for other seasons (not shown) has similar dipole structure but the explained variance is smaller (e.g., 53.4% in summer, 69.3% in winter, 54.5% in spring).

The principal component (PC) for the subsurface dipole mode in SON is displayed in Fig. 3b. Large negative excursions (i.e. cold in the east and warm in the west) occurred in 1961, 1994, and 1997, which are years previously identified by Saji et al. (1999) and Webster et al. (1999) as surface dipole years. Large positive excursions (warm in the east and cold in the west) occurred in 1984 and 1995, which were also previously identified as oppositely-signed surface dipole years. Also shown in Fig. 3b is the time series of the Nino3.4 index (note sign is flipped in plot). While some large ENSO events are detectable in the PC time series (e.g., 1982, 1997), large subsurface dipole events also occur in the absence of ENSO (e.g., 1961, 1984) and some ENSO events are not evident in the PC time series (e.g., 1965, 1987, 1988). This is reflected in the modest correlation of the two time series (-0.37, Table 1). Note that the lag

correlation between the PC in SON and the Nino3.4 SST in JJA is lower (-0.23).

The evolution of the subsurface dipole has previously been shown to be governed by Rossby and Kelvin waves forced by near-equatorial zonal winds (e.g., Murtugudde and Bussalacchi 1999; Rao et al. 2002). The tight coupling to the equatorial zonal wind is demonstrated by the high correlation of the zonal wind in the central Indian Ocean (averaged 70°E-90°E, 5°N-5°S) with the subsurface dipole mode (0.9, Table 1). The association with Rossby and Kelvin waves is inferred from the correlation of the PC of the subsurface dipole mode with D20 anomalies over the Indian Ocean (Fig. 4a). This structure is consistent with the adjustment of the thermocline to imposed zonal winds across the center of basin (e.g., McCreary and Anderson 1984). In association with enhanced equatorial westerlies (Fig. 3b), the elevated thermocline in the western Indian Ocean takes the form of an upwelling Rossby wave, with equatorially-symmetric height anomalies centered at about 70°E. To the east, the suppressed thermocline takes the form of downwelling Kelvin wave, which travels poleward along the eastern boundary as a coastally trapped Kelvin wave and also reflects resulting in westward propagating downwelling Rossby waves. Note that further analyses are required for the complete description of propagation and reflection of these waves.

The expression of the subsurface dipole at the surface is indicated by the correlation of the PC of the subsurface dipole mode with SST (Fig. 4b). The structure of the dipole in the subsurface is nearly equatorially symmetric (Fig. 4a), whereas the surface expression is skewed to the southern hemisphere. This SST structure is similar to that of the the surface dipole identified by Saji et al (1999) and Webster et al. (1999) and to the leading EOF of SST during SON (e.g., Fig. 1 and Shinoda et al. 2003). The strong correlations between local SST and the subsurface dipole (i.e., magnitude greater than 0.8 in the east and 0.7 in the west) suggest that subsurface

dynamics may play a prominent role for driving SST variations.

EOFs are also computed for the model SST anomalies in the Indian Ocean. The leading EOF for SON (Fig. 5a), which captures 41.4% of the variance, also has dipole structure that is similar to observed (Fig. 1) and to that associated with the subsurface dipole (Fig. 4b). The PC of the leading EOF of model SST along with Nino3.4 are shown in Fig. 5b. In contrast to the subsurface dipole (Fig. 3b), the surface dipole is strongly correlated with Nino3.4 (correlation -0.65, Table 1). This high correlation is consistent with other observational analyses that have indicated a strong connection between ENSO and development of a surface dipole in boreal autumn (e.g., Baquero-Banal et al. 2002, Hendon 2003, Shinoda et al. 2003). But, some surface dipole events occur in the absence of ENSO conditions in the Pacific (e.g., 1961) and some ENSO events are not associated with a pronounced surface dipole (e.g., 1965).

This occurrence of surface dipole variations that are independent from ENSO appears to stem from subsurface dipole variations that are forced by zonal wind variations that are also independent of ENSO. This is seen by first considering that the SST dipole is well correlated with the subsurface dipole mode (correlation = 0.78, Table 1), which emphasizes the prominent role of subsurface dynamics for driving SST variations. The partial correlation of the leading EOF of SST with the subsurface dipole, where the linear relationship with Nino3.4 SST is removed, is also large (partial correlation=0.76, Table 1). This suggests that subsurface dipole variations that are independent of ENSO are responsible for the surface dipole variations that occur in the absence of ENSO. This is substantiated by the strong partial correlation of the subsurface dipole with the surface zonal wind once the effects of Nino3.4 have been removed (partial correlation=0.87, Table 1). This high correlation is consistent with the somewhat weaker relationship between zonal wind and ENSO (r(Nino3.4,u)=-0.6,

Table 1) and that the surface dipole and zonal wind are still related (partial correlation=0.69, Table 1) even after the effects of Nino3.4 are removed. One interpretation of this analysis is that surface zonal wind variations both dependent and independent of ENSO are the primary driver of subsurface variability in the Indian Ocean. The zonal wind anomalies are driven both remotely by ENSO (correlation -0.6, Table 1) and locally by anomalous SST gradient in the Indian Ocean (correlation 0.81, Table 1). However, it appears that the manner in which ENSO remotely forces the zonal wind over the Indian Ocean is through the induced SST anomaly in the Indian Ocean because the correlation of zonal wind with Nino3.4 disappears if the effects of the surface dipole are removed (partial correlation -0.18, Table 1). On the other hand, the surface dipole in the Indian Ocean can develop during ENSO but independent of the subsurface dipole, as the partial correlation of Nino3.4 and the surface dipole is still high after the effects of the subsurface dipole are removed (partial correlation -0.61, Table 1).

4. Composite evolution of upper ocean

In the previous section, we showed that near-equatorial subsurface variability in the Indian Ocean during SON is dominated by a zonal dipole, which is more independent of ENSO than is the dipole variability at the surface. However, the ENSO-independent dipole variation of SST is evident. Furthermore, there is a nonlinear relationship between the strength of ENSO and the strength of the SST dipole during SON: some large ENSO events are associated with modest dipoles while some modest ENSO events are associated with strong dipoles. It is possible that different mechanisms are involved in producing surface dipole variability, and these mechanisms may or may not be associated with all ENSOs. To explore these issues, we examine the subsurface and surface evolution in the Indian Ocean during ENSO and contrast that to what occurs in association with subsurface dipole variations. We do so by creating composites based on occurrence of ENSO and on occurrence of the subsurface dipole. The upper ocean heat budget is calculated in order to elucidate the important processes that control the evolution of SST in each case.

4.1. Evolution of SST, thermocline depth and winds

Composites are formed based on 7 El Nino events (1965, 1969, 1972, 1976, 1982, 1987, 1991) and 5 La Nina events (1964, 1970, 1973, 1975, 1988). These periods were selected by Lau and Nath (2000) using the criteria that the monthly SST anomaly in the 5°S-5°N, 120-150°W region exceeded the 0.4°C threshold for a duration of more than 12 months. Note that 1997 is excluded from El Nino years since the model experiment ends in December 1997 and thus the entire period of this ENSO event (97/98) cannot be included in the composite. We refer to these years as Year(0), and the following years as Year(1). Averages over El Nino events and La Nina events

for each variable are first computed. Then the composite El Nino minus La Nina conditions are calculated, which is referred to as "ENSO composite" hereafter.

Positive and negative subsurface dipole years are identified by excursions greater than 1 standard deviation of the PC time series for the subsurface dipole mode. Composites are formed for positive dipole years and negative dipole years. Their difference (positive minus negative) is referred to as the "subsurface dipole composite". None of the positive dipole years (1961, 1963, 1967, 1994) include major El Nino year, and the negative dipole years (1971, 1975, 1984, 1996) only includes one La Nina event. Hence, the subsurface dipole composite is mostly ENSO-independent. In order to assess the sensitivity of the composite to the large ENSO event in 1997, which is associated with the large subsurface dipole, we also formed the composites including this year (not shown). The results are qualitatively similar and our major conclusions obtained from the composite analysis are not affected.

The subsurface dipole composites of D20 and surface winds are shown in Fig. 6 for the JJA and SON seasons in Year(0) and the following DJF and MAM seasons in Year(1). Beginning in JJA, south-easterly surface winds across the eastern Indian Ocean generate an eastward propagating Kelvin wave, which elevates the thermocline to the east. Upon reaching the eastern boundary, this wave propagates poleward in both hemispheres as a coastally trapped Kelvin wave. The easterlies also generate a downwelling Rossby wave to the west, with gyres centered at 5-10° latitude. The greatest zonal contrast across the basin occurs in SON, in association with the strongest south easterly surface winds. The south easterlies also induce upwelling along the Sumatra and Java coasts, adding to the elevation of the thermocline induced by the equatorial waves. By DJF, the southeasterly anomalies have decreased and the initial Kelvin wave has reflected off the eastern boundary, generating upwelling Rossby gyres that propagate westward. By MAM, some evidence of a reflected Kelvin

wave appears in the central part of the eastern basin, emanating from arrival of the original downwelling Rossby wave at the African coast. However, the thermocline perturbations seem to decay because the surface winds that force them begin to decay in DJF, long before arrival of this downwelling Kelvin wave has a chance to affect the SST in the eastern Indian Ocean.

The associated SST evolution is shown in Fig. 7. A SST dipole occurs in association with the subsurface dipole in SON. However, the SST anomaly in the east is more than twice as strong as in the west. The evolution of SST in the eastern portion of the basin is similar to that of D20, suggesting a strong dynamical control on the SST evolution. SST anomalies in the eastern portion of the basin are also much stronger south of the equator, while the D20 anomalies are more equatorially symmetric, discussed further in section 4.2. By DJF, the SST anomaly in the east is dramatically reduced, while the oppositely signed anomalies in the west maintain their amplitude. Hence, the greatest zonal gradient occurs in SON. By MAM the anomalies have weakened across the entire basin, with little remaining evidence of the dipole at the surface.

The evolution of D20 and SST associated with ENSO is shown in Figs. 8 and 9. While the structure and evolution of the D20 anomalies (Fig. 8) shows some similarities with those associated with the subsurface dipole, the amplitude is weaker. Furthermore, the easterly wind anomalies are weaker, especially in JJA. The SST anomaly exhibits a similar dipole structure that peaks in SON, but, in contrast to the subsurface dipole composite, it gives way to a basin-scale warm anomaly by DJF (e.g., Klein et al. 1999). The spatial structure of the SST dipole anomaly during ENSO is also different than that associated with the subsurface dipole. During ENSO, the SST anomaly in the eastern Indian Ocean extends farther south ($\sim$20°S), and there is almost no negative anomaly near the equator. Also, there appears to be less of a

control of the SST by the subsurface variations. For instance negative SST anomalies show up in the east during JJA before there is evidence of an elevated thermocline there. In addition, SSTs become warm in the east in DJF, while the subsurface is still cold. These structure and evolution of SST anomalies associated with ENSO are further confirmed by the regression analyses (Appendix).

These differences are highlighted by vertical sections of the composite temperature anomalies in the eastern Indian Ocean (Fig. 10). Distinctly different variations above ∼30m and below ∼30m in the eastern Indian Ocean is seen in the ENSO composite, indicating little control of the SST by the subsurface. On the other hand, the subsurface (below ∼30m) temperature anomaly and SST anomaly are almost in-phase for the subsurface dipole case, suggesting a strong control of the SST by the subsurface variation.

Some of these differences are summarized in Fig. 11, which shows the zonal wind in the central Indian Ocean, D20 and SST anomalies in the eastern Indian Ocean, and Nino3.4 for the subsurface dipole and ENSO composites. These composite anomalies are consistent with the composite formed by Rao et al. (2002) who used different ENSO and dipole years. Strong easterly anomalies in the central Indian Ocean begin in early summer for the subsurface dipole composite. They generate the large D20 anomaly during summer and fall, which is reflected in the SST anomaly. The easterly anomalies begin later for the ENSO composite and are about a half as strong as those for the dipole composite. Although zonal wind anomalies during SON are well correlated with ENSO (Table 1), they generate the relatively small subsurface anomaly in late fall to early winter. Furthermore, the SST evolution shows little connection with the subsurface variation, especially when the SST begins to warm in December.

4.2. Heat budget

We calculate the upper ocean heat budget in the eastern and western Indian Ocean in order to identify the dominant processes that control the interannual variations of SST during ENSO and during subsurface dipole events. The climatological mixed layer in this region is shallower than 30m most of the time (e.g., Monterey and Levitus 1997), thus the heat budget of upper 30m is analyzed.

The surface heat flux, vertical and horizontal heat advection and temperature tendency in the upper ocean in the eastern and western Indian Ocean are shown in Fig. 12 for the subsurface dipole and ENSO composites. The temperature tendency is calculated from the composite temperature. Note that the anomaly of shortwave radiation, a prominent component of the surface heat flux (e.g., Hendon 2003), is negligible since climatological values are prescribed for most of the period (Sec. 2). Thus, the surface heat flux variation is primarily caused by the latent heat flux. This result is further confirmed by the regression analysis (Appendix).

In the eastern Indian Ocean, surface heat fluxes are the dominant term in the heat budget for the ENSO composite, corroborating previous studies that have indicated that dipole variations are primarily controlled by surface heat fluxes (e.g., Hendon 2003, Shinoda et al. 2003). Increased latent heat flux (evaporative cooling) from July to September acts to cool the surface while decreased latent heat flux from November to February acts to warm the surface. The warming beginning in November is also promoted by positive horizontal advection, which is generated by the mean positive zonal gradient of SST and an anomalous westward current driven by anomalous easterlies during October-January. Vertical advection (upwelling), which is strongest October and November, opposes the horizontal advection and, in fact, is out of phase with the mixed layer temperature tendency.

For the subsurface dipole composite, initial cooling in the east during July is caused by negative surface heat flux anomaly and upwelling. However, the surface heat flux then becomes positive, with the strongest cooling during August and September resulting from upwelling and horizontal advection. The anomalous vertical advection (upwelling) corresponds to the largest D20 anomaly (Fig. 11). As for the ENSO composite, the subsequent warming from October onwards is largely driven by increased surface heat flux and positive horizontal temperature advection, while upwelling acts to cool. The important role of surface heat flux in the SST evolution associated with ENSO is further confirmed by the regression analysis (Appendix).

The marked contrast of the surface heat flux during August through October for the ENSO and subsurface dipole cases results from the differing latent heat flux anomalies. In both cases, the surface wind anomaly is easterly, which increases the windspeed. For the ENSO case, this increases the latent heat flux. Despite the increased windspeed, the latent heat flux decreases for the dipole case because of the sharp decrease in SST, which lowers the saturated specific humidity at the surface.

Interpretation of the heat budget in the western Indian Ocean is not as simple as in the east. In general, all processes are important. The surface heat flux contributes most to the warming during fall for the ENSO composite. For the dipole composite, horizontal advection of heat is significant during September-October, vertical advection becomes large during November, and the surface heat flux becomes negative in December and January.

The large surface cooling in the eastern Indian Ocean for the subsurface dipole composite mostly occurs south of the equator, while significant D20 anomalies are also evident north of the equator. The composite heat budget north of the equator (10°N-equator, 90°E-100°E) (not shown) shows that vertical advection during August-September is about half of that in the Southern Hemisphere and horizontal advection

warms the surface layer during subsurface dipole events. Also, substantial differences of the surface heat flux between northern and southern hemispheres occur during July. The surface heat flux anomaly contributes significantly to the initial cooling in the southern hemisphere during July, while the anomalous surface heat flux in the northern hemisphere acts to warm. This difference is primarily caused by the wind speed anomaly, which is positive (higher wind speed) in the Southern Hemisphere and negative in the Northern Hemisphere during this month.

The above analyses suggest that there are two varieties of SST dipole: one is governed by the surface heat flux variations remotely forced by ENSO and the other is governed by wind-driven ocean dynamics that are largely independent of ENSO. In both cases, occurrence of the surface dipole in SON is accompanied by easterly anomalies in the equatorial Indian Ocean, which force Rossby and Kelvin waves. D20 and SST anomalies are relatively large and co-evolve during subsurface dipole events, while the SST tends to evolve independent of the subsurface during most ENSO events. Strong easterly anomalies in the central Indian Ocean, which begin during boreal summer, drive large D20 anomalies in the eastern Indian Ocean during subsurface dipole events. On the other hand, the latent heat flux anomaly in the eastern Indian Ocean is primarily determined by local winds and SSTs. The wind speed anomaly in the eastern Indian Ocean associated with ENSO has same sign and is about a half in magnitude to that during subsurface dipole events, but the eastern Indian Ocean SST anomaly is weaker. Hence, easterly anomalies promote similar subsurface anomalies in the two cases but the latent heat flux has opposite sign.

Since the large anomalies of subsurface (D20) occur during non-ENSO years (e.g., 1961, 1967, 1994) as discussed above and the subsurface anomaly is relatively small during ENSO years (Fig. 11), subsurface EOF is not well correlated with ENSO (Table 1). On the other hand, the large SST dipole is developed in both

ENSO-independent subsurface dipole years and most of the ENSO years, and thus the SST dipole is well correlated with both ENSO and the subsurface dipole (Table 1). As discussed above, the large SST anomalies are generated primarily by subsurface variability during non-ENSO years and by surface heat fluxes during ENSO years.

5. Conclusions

Surface and subsurface temperature variability in the equatorial Indian Ocean and its relation to ENSO was examined using output from an OGCM forced with observed surface fluxes. Emphasis was given to dipole variations, which are prominent in SON at the surface but occur year round in the subsurface. The surface dipole is strongly correlated with ENSO, while the subsurface dipole is mostly independent of ENSO.

Composites based on occurrences of ENSO and the subsurface dipole were formed to highlight the differing evolutions. The composite upper ocean heat budget indicates that ENSO typically induces a relatively shallow surface dipole that is primarily controlled by surface heat flux variations. Wind-forced ocean dynamics play an important role for the SST dipole that accompanies the subsurface dipole. In particular, cooling in summer in the eastern Indian Ocean is generated by strong upwelling and horizontal heat advection, which is opposed by decreased latent heat flux. In contrast, the cooling is driven by increased latent heat flux during ENSO, with less role for subsurface dynamics. In both cases, surface warming in the eastern Indian Ocean during October-December stems from decreased upward latent heat flux and positive horizontal temperature advection, with vertical advection (upwelling) acting to oppose the warming.

Many subsurface dipole events occur independent of ENSO but some ENSO events are associated with large subsurface dipoles. This suggests that the ENSO-induced surface zonal wind anomalies in the Indian Ocean can sometimes trigger a dynamically-controlled dipole. However, surface zonal winds over the Indian Ocean are to some extent independent of ENSO. It is unclear whether these ENSO-independent variations of winds are coupled to the SST variations that they generate in the Indian Ocean, as suggested in Sec. 3, or whether the SST variation is just a response to the

winds. Coupled modeling studies are required to assess this. Furthermore, basin-scale surface zonal wind variations are generated by other phenomena including variations in the Australian and Indian summer monsoons and by the MJO (Madden and Julian 1972). Further study is required to ascertain their role in generating dipole variability in the Indian Ocean.

Appendix. Regression of Indian Ocean SST and upper ocean heat budget onto Nino3.4 SST

In order to confirm the spatial structure and time evolution of SST anomalies associated with ENSO described by the ENSO composite, the Indian Ocean SSTs are regressed onto the Nino3.4 SST during SON (Fig. 13). The seasonal evolution of SST anomaly is similar to the ENSO composite (Fig. 9). The negative SST anomalies associated with ENSO start developing during JJA, and the SST dipole structure peaks in SON. The basin-scale warm anomaly is then developed in DJF.

In order to remove the effect of subsurface dipole variability on the SST anomalies, the linear relationship of SSTs with PC-1 (from subsurface temperature) is first removed from the SST time series. Then the same regression onto the Nino3.4 are calculated (Fig. 14). The spatial structure of the SST dipole during SON is fairly similar to that in Fig. 13. However, the magnitude is smaller. Since the PC-1 is moderately correlated with Nino3.4 SST (r=-0.37), a significant portion of ENSO-induced variability may be removed from the SST time series.

Upper ocean temperature, horizontal and vertical advection of heat and surface heat flux in the eastern Indian Ocean are also regressed onto Nino3.4 SST during SON (not shown). The seasonal evolution of each variable is similar to the composite heat budget shown in Fig. 12a, suggesting that SST anomalies associated with ENSO in the eastern Indian Ocean are primarily controlled by surface heat fluxes. Figure 15 shows spatial structures of the regression of surface heat flux and vertical heat advection during July-September. The cooling anomalies of surface heat flux in the eastern Indian Ocean extends to $\sim$20°S, which is consistent with the structure of the ENSO composite SST anomaly. The large vertical advection of heat is confined to narrow regions near the coast of Java and Sumatra.

Acknowledgment

Support for this work was provided by CLIVAR-Pacific Grants from NOAA's office of Global Programs.

References

Alexander, M. A., I. Blade, M. Newman, J. Lanzante, N.-C. Lau, and J. Scott, 2002: The atmospheric bridge: the influence of ENSO teleconnections on air-sea interaction over the global oceans. J. Climate, 15, 2205-2231.

Baquero-Bernal, A., M. Latif, and S. Legutke, 2002: On dipolelike variability of sea surface temperature in the tropical Indian Ocean. J. Clim., 15, 1358-1368.

Behera, S. K, P. S. Salvekar, and T. Yamagata, 2000: Simulation of interannual SST variability in the tropical Indian Ocean. J. Clim., 13, 3487-3499.

Bishop, J. K. B., and W. B. Rossow, 1991: Spatial and temporal variability of global surface solar irradiance. J. Geophys. Res., 96, 16839-16858.

Chambers, D. P., B. D. Tapley, and R. H. Stewart, 1999: Anomalous warming in the Indian Ocean coincident with El Nino. J. Geophys. Res., 104, 3035-3047.

Flohn, H., 1986: Indonesian droughts and their teleconnections. Berliner Geographishe Studien, 20, 251-265.

Gent, P. R., and J. C. McWilliams, 1990: Isopycnal mixing in ocean circulation models. J. Phys. Oceanogr., 20, 150-155.

Gent, P. R., F. O. Bryan, G. Danabasoglu, S. C. Doney, W. G. Holland, W. G. Large, and J. C. McWilliams, 1998: The NCAR Climate System Model global ocean component. J. Phys. Oceanogr., 11, 1287-1306.

Hastenrath, S., A. Nicklis and L. Greischar, 1993: Atmospheric-hydrospheric mechanisms of climate anomalies in the western equatorial Indian Ocean. J. Geophys. Res., 98, 20219-20235.

Hastenrath, S., 2002: Dipoles, temperature gradients, and tropical climate anomalies. Bull. Amer. Meteor. Soc., 83, 735-738.

Hendon H. H., 2003: Indonesian rainfall variability: Impact of ENSO and local air-sea interaction. J. Climate, 16, 1775-1790.

Kalnay, E., and Co-authors, 1996: The NCEP/NCAR 40-Year Reanalysis Project. Bull. Amer. Meteor. Soc., 77, 437-471.

Klein, S. A., B. J. Soden and N. C. Lau 1999: Remote sea surface temperature variations during ENSO: Evidence for a tropical atmospheric bridge. J. Climate., 12, 917-932.

Large, W. G., J. C. McWilliams and S. C. Doney, 1994: Oceanic vertical mixing: Review and a model with a nonlocal boundary layer parameterization. Rev. Geophys., 32, 363-403.

Large, W. G., G. Danabasoghu, and S. C. Doney, 1997: Sensitivity to surface forcing and boundary layer mixing in a global ocean model: annual-mean climatology. J. Phys. Oceanogr., 27, 2418-2447.

Large, W. G., J. C. McWilliam, P. R. Gent, and F. O. Bryansand, 2001: Equatorial circulation of a global ocean climate model with an isotropic horizontal viscosity. J. Phys. Oceanogr., 31, 518-536.

Large, W. G., and S. Pond, 1982: Sensible and latent heat flux measurements over the ocean. J. Phys. Oceanogr., 12, 464-482

Latif, M., and T. P. Barnett, 1995: Interactions of the Tropical Oceans. J. Climate, 8, 952-964.

Lau, N. C. and M. J. Nath 2000: Impact of ENSO on the variability of the Asian-Australian monsoons as simulated in GCM experiments. J. Climate, 13, 4287-4309.

Lau, N. C. and M. J. Nath 2003: Atmosphere-ocean variations in the Indo-Pacific sector during ENSO episode. J. Climate, 16, 3-20.

Madden, R. A., and P. R. Julian, 1972: Description of global-scale circulation cells in the tropics with a 40-50 day period. J. Atmos. Sci., 29, 1109-1123.

McCreary, J. P., and D. T. Anderson, 1984: Simple models of El Nino and the Southern Oscillation. Mon. Wea. Rev., 112, 934-946.

Monterey, G. I., and S. Levitus, 1997: Climatological cycle of mixed layer depth in the world ocean. U.S. Gov. Printing Office, NOAA Nesdis, 5pp.

Murtugudde, R., and A. J. Bussalacchi, 1999: Interannual variability of the dynamics and thermodynamics of the tropical Indian Ocean. J. Climate, 12, 2300-2326.

Murtugudde, R., J. P. McCreary Jr. and A. J. Bussalacchi, 2000: Oceanic processes associated with anomalous events in the Indian Ocean with relevance to 1997-1998. J. Geophys. Res., 105, 3295-3306.

Paulson, C. A., and J. J. Simpson, 1977: Irradience measurements in the upper ocean, J. Phys. Oceanogr., 7,952-956.

Rasmusson, E. M., and T. H. Carpenter, 1982: Variations in tropical sea surface temperature and surface wind fields associated with the Southern Oscillation/El Nino. Mon. Wea. Rev., 110, 354-384.

Rao, S. A., S. K. Behera, Y. Masumoto, and T. Yamagata, 2002: Interannual subsurface variability in the tropical Indian Ocean with a special emphasis on the Indian Ocean dipole. Deep Sea Res. II, 49, 1549-1572

Reverdin, G., D. Cadet and D. Gutzler, 1986: Interannual displacements of convection and surface circulation over the equatorial Indian Ocean. Q. J. R. Met. Soc., 112, 43-67.

Reynolds, R. W. and T. M. Smith, 1994: Improved global sea surface temperature analyses using optimum interpolation. J. Climate, 7, 929-948.

Rossow, W.B., and R. A. Schiffer, 1991: ISCCP cloud data products. Bull. Amer. Meteor. Soc., 72, 2-20.

Saji, N. H., B. N. Goswami, P. N. Vinayachandran and T. Yamagata 1999: A dipole mode in the tropical Indian Ocean. Nature, 401, 360-363.

Shinoda, T., M. A. Alexander, and H. H. Hendon 2003: Remote response of the Indian Ocean to interannual SST variations in the tropical Pacific. J. Climate (submitted)

Smith, T. M., R. W. Reynolds, R. E. Livezey, and D. C. Strokes, 1996: Reconstruction of historical sea surface temperatures using empirical orthogonal functions. J. Clim., 9, 1403-1420.

Spencer, R.W., 1993: Global oceanic precipitation from the MSU during 1979-91 and comparisons to other climatologies. J. Clim., 6, 1301-1326.

Vinayachandran, P. N., S. Iizuka, and T. Yamagata, 2002: Indian Ocean dipole mode events in an cean eneral circulation model. Deep Sea Res. II, 49.

Venzke, S., M. Latif and A. Villwock 2000: The coupled ECHO-2. Part II: Indian ocean response to ENSO. J. Clim., 13, 1371-1383.

Webster, P. J., A. M. Moore J. P. Loschnig and R. R. Leben 1999: Coupled ocean-atmosphere dynamics in the Indian Ocean during 1997-98. Nature, 401, 356-360.

White, W. B., S. E. Pazan, G. W. Withee, and C. Noe, 1998: Joint Environmenta Data Analysis (JEDA) center for scientific quality control of upper ocean thermal data in support of TOGA and WOCE. EOS transactions, American Geophysical Union, 69m122-123

Xie, P., and P. A. Arkin, 1996: Analysis of global monthly precipitation using gauge observations, satellite estimates and numerical model predictions. J. Clim., 9, 531-544.

Xie, S. P., H. Annamalai, F. A. Schott and J. P. McCreary 2001: Structure and mechanism of south Indian Ocean climate variability. J. Clim., 15, 864-878.

Table 1: Correlation coefficients between PC(subsurface), PC(SST), zonal winds, and Nino3.4 SST during SON. The values with parentheses indicates partial correlations where linear relationship with the variable in parentheses is removed (see text for details)

	PC-1(subsurface)	PC-1(SST)	Zonal winds	Nino34
PC(subsurface)	1.0	0.76(Nino34)	0.87(Nino34)	
PC(SST)	0.78	1.0	0.69(Nino34)	-0.62(subsurface)
Zonal winds	0.87	0.81	1.0	-0.18(SST) -0.61(subsurface)
Nino34	-0.37	-0.65	-0.60	1.0

Figure captions

Figure 1: (a) The first eigenvector of the SST analysis (Reynolds and Smith 1994). (b) PC-1 (solid line) and Nino3.4 SST anomaly (dotted line). Time series are normalized by their standard deviations.

Figure 2: (a) Time series of SST anomaly from observations (dashed line) and the model (solid line) in the western Indian Ocean (50°E-70°E, 10°S-10°N) (upper panel) and the eastern Indian Ocean (90°E-110°E, 10°S-0) (lower panel) (b) Same as (a) except for the 20°C isotherm depth anomaly.

Figure 3: (a) The first eigenvector of the temperature of longitude-depth plane for September-November. (b) PC-1 (solid line), Nino34 SST anomaly (dotted line) and zonal winds in the central Indian Ocean (70°E-90°E, 5°N-5°S) for September-November. The sign of Nino3.4 SST is changed for the comparison.

Figure 4: Correlation coefficients of D20 (upper panel) and model SST (lower panel) with PC-1 from the EOF analysis of temperature in the equatorial longitude-depth plane.

Figure 5: (a) The first eigenvector of the model SST. (b) PC-1 of the EOF analysis of model SST and Nino3.4 SST anomaly. Time series are normalized by their standard deviations. The sign of Nino3.4 SST is changed.

Figure 6: The subsurface dipole composite (see text for the detail) of 20°C isotherm depth and surface winds during June-August (a), September-November (b), December-

February (c), and March-May (d).

Figure 7: The subsurface dipole composite of SST during June-August (a), September-November (b), December-February (c), and March-May (d).

Figure 8: The ENSO composite (see text for the detail) of 20°C isotherm depth and surface winds during June-August (a), September-November (b), December-February (c), and March-May (d).

Figure 9: The ENSO composite of SST during June-August (a), September-November (b), December-February (c), and March-May (d).

Figure 10: (a) The ENSO composite (upper panel) and dipole composite (lower panel) of the average temperature in the eastern Indian Ocean (90°E-110°E, 10°S-0).

Figure 11: The subsurface dipole composite (upper panel) and ENSO composite (lower panel) of zonal winds (closed square) in the central Indian Ocean (70°E-90°E, 5°N-5°S), D20 (closed circle) and SST (triangle) in the eastern Indian Ocean, and Nino3.4 SST anomaly (diamond). The ordinates on the left side of the panel are for the SST in the eastern Indian Ocean (left) and for Nino3.4 SST (center).

Figure 12: (a) Upper panel: The ENSO composite of SST tendency (open circle), vertical advection of heat (closed circle), horizontal advection of heat (triangle) in the upper 30 m and net surface heat flux (closed square) in the eastern Indian Ocean. Lower panel: Same as the upper panel except for the subsurface dipole composite. (b) Same as (a) except for the western Indian Ocean.

Figure 13: SST anomalies during JJA (a), SON (b) and DJF (c) regressed onto Nino3.4 SST during SON.

Figure 14: Same as Fig. 13b except the linear relationship of SST anomalies with PC-1 (from the subsurface temperature) is removed.

Figure 15: Surface heat flux (a) and vertical advection of heat (b) during July-August regressed onto Nino3.4 SST (SON).

Fig. 1

(a)

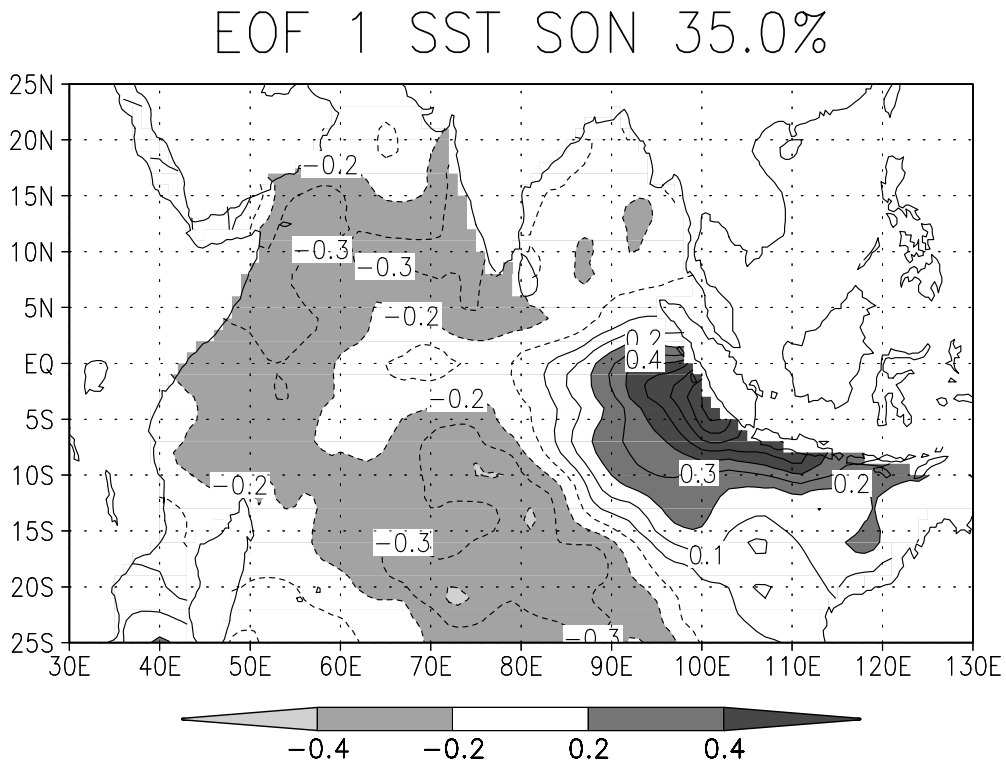
EOF 1 SST SON 35.0%
25N
20N
15N
10N
5N
EQ
5S
10S
15S
20S
25S
30E
40E
50E
60E
70E
80E
90E
100E
110E
120E
130E
−0.2
−0.3
−0.3
−0.2
0.2
0.4
−0.2
−0.2
0.3
0.2
−0.3
0.1
−0.4
−0.2
0.2
0.4

Fig. 1

(b)

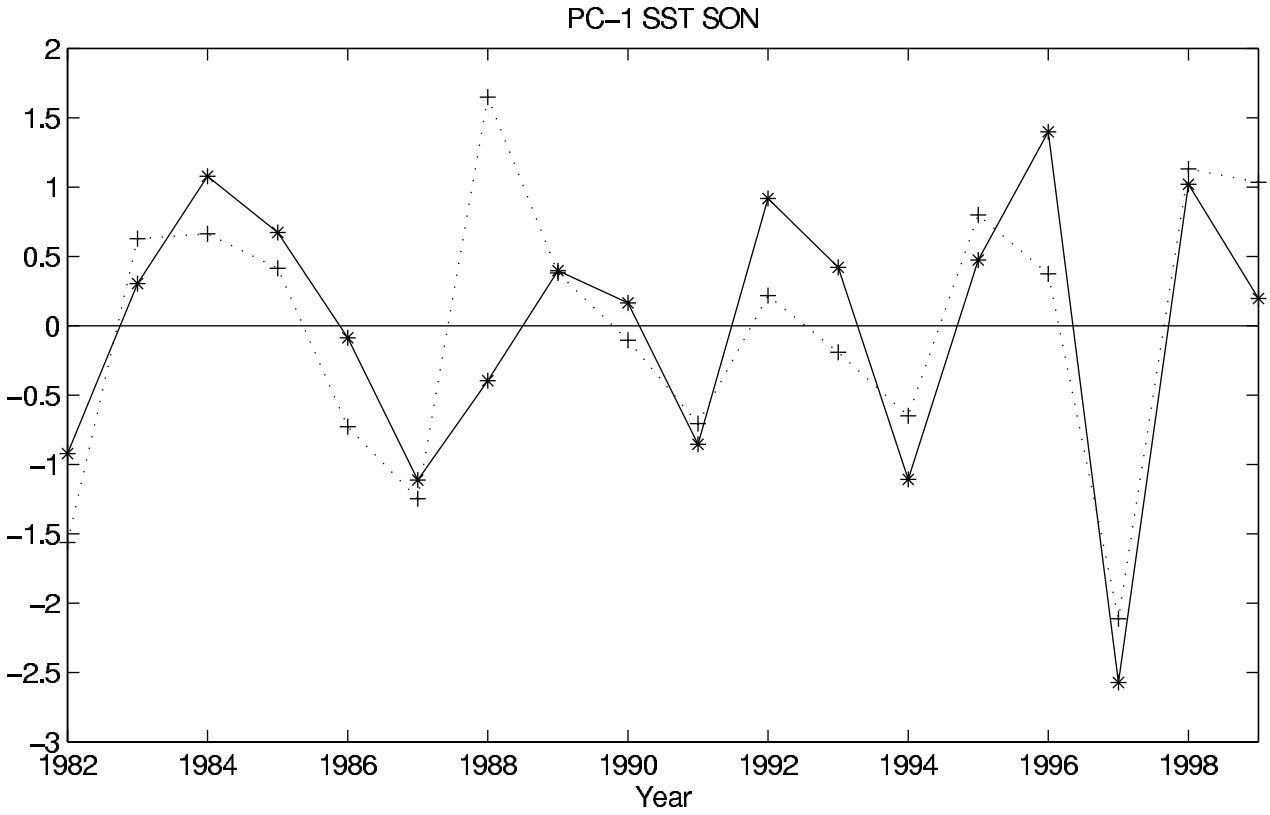
PC−1 SST SON
2
1.5
1
0.5
0
−0.5
−1
−1.5
−2
−2.5
−3
1982
1984
1986
1988
1990
1992
1994
1996
1998
Year

Fig. 2

(a)

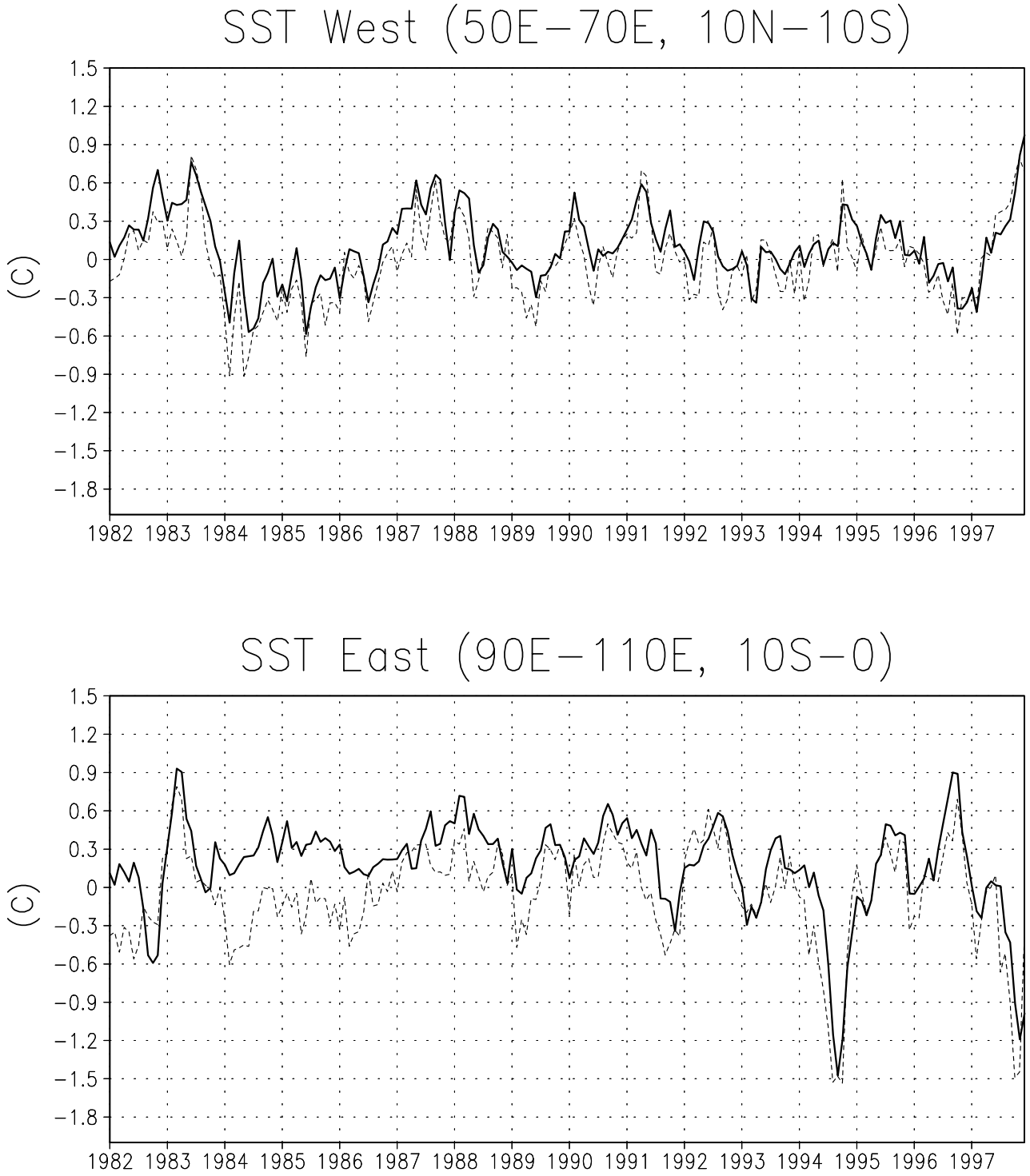
SST West (50E−70E, 10N−10S)
(C)
1.5
1.2
0.9
0.6
0.3
0
−0.3
−0.6
−0.9
−1.2
−1.5
−1.8
1982 1983 1984 1985 1986 1987 1988 1989 1990 1991 1992 1993 1994 1995 1996 1997
SST East (90E−110E, 10S−0)
(C)
1.5
1.2
0.9
0.6
0.3
0
−0.3
−0.6
−0.9
−1.2
−1.5
−1.8
1982 1983 1984 1985 1986 1987 1988 1989 1990 1991 1992 1993 1994 1995 1996 1997

Fig. 2

(b)

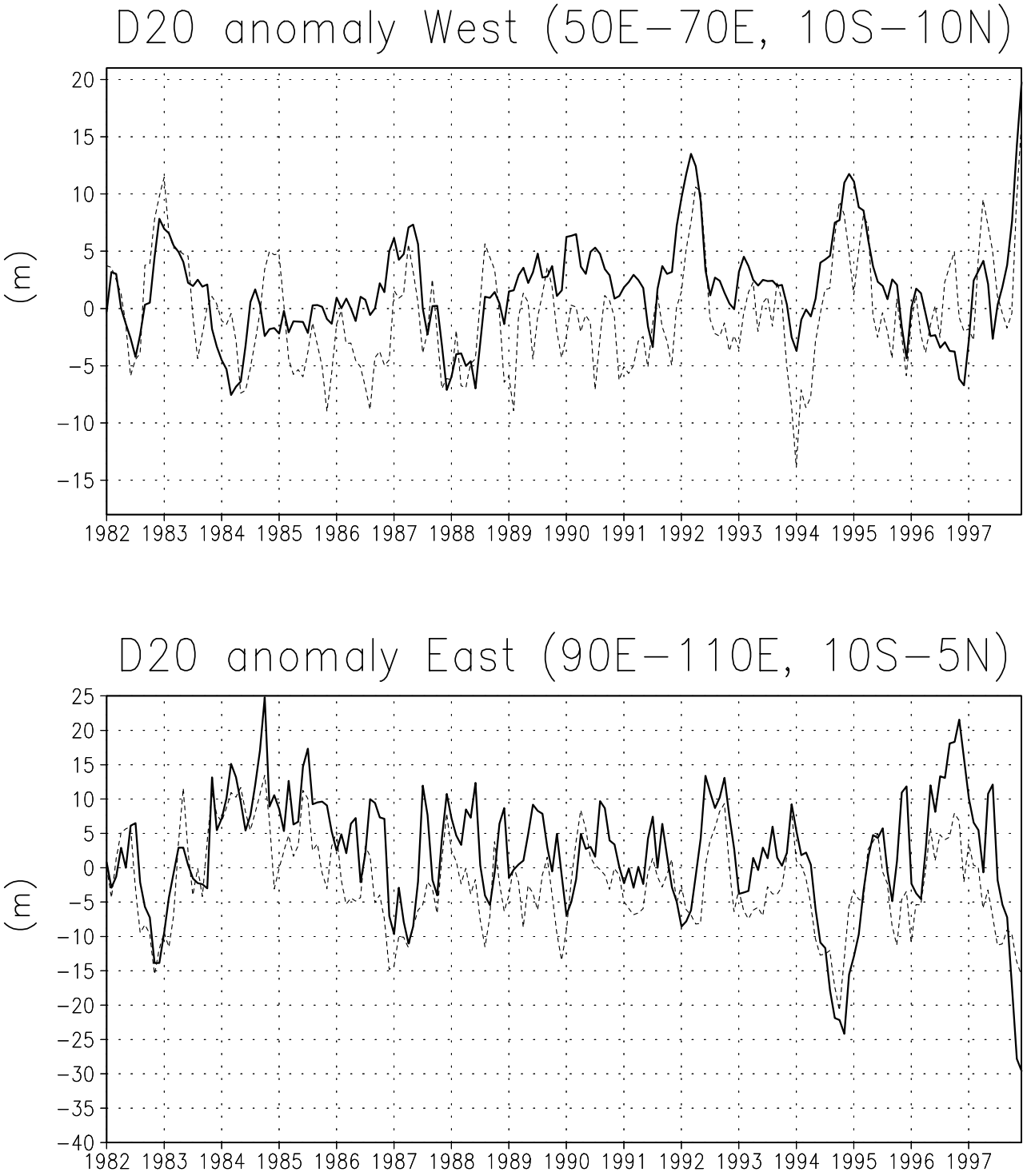
D20 anomaly West (50E−70E, 10S−10N)
(m)
20
15
10
5
0
−5
−10
−15
1982 1983 1984 1985 1986 1987 1988 1989 1990 1991 1992 1993 1994 1995 1996 1997
D20 anomaly East (90E−110E, 10S−5N)
(m)
25
20
15
10
5
0
−5
−10
−15
−20
−25
−30
−35
−40
1982 1983 1984 1985 1986 1987 1988 1989 1990 1991 1992 1993 1994 1995 1996 1997

Fig. 3

(a)

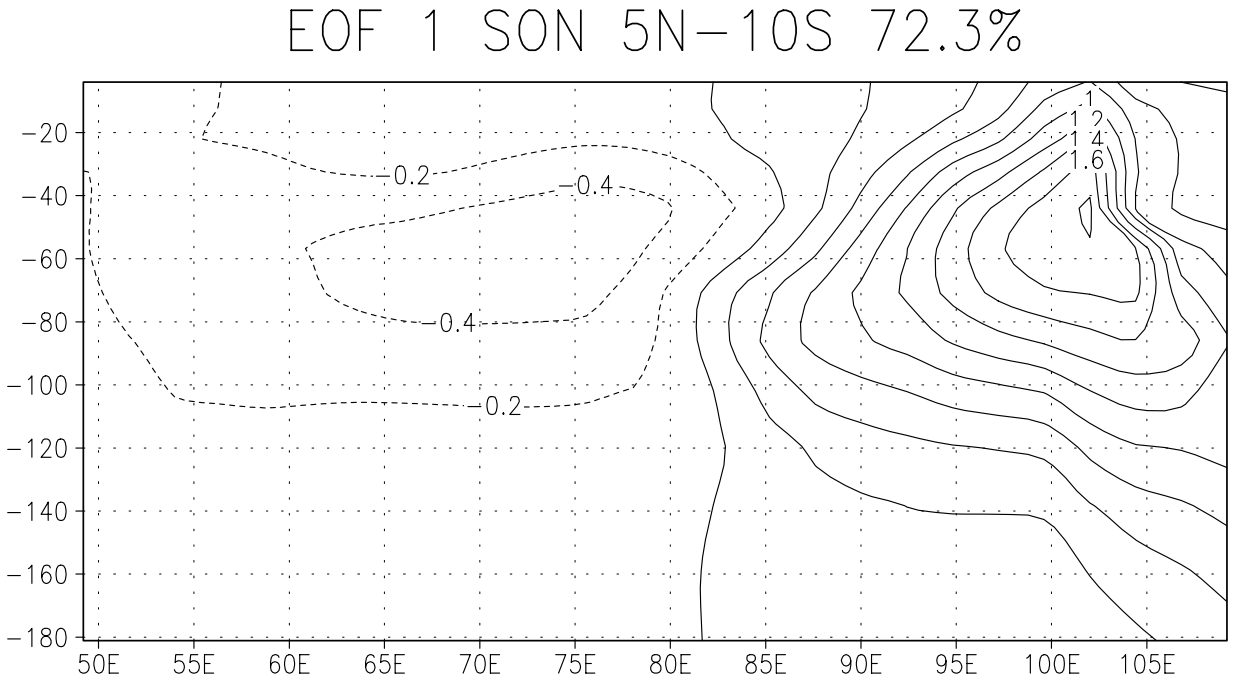
EOF 1 SON 5N−10S 72.3%
−20
−40
−60
−80
−100
−120
−140
−160
−180
50E
55E
60E
65E
70E
75E
80E
85E
90E
95E
100E
105E
0.2
0.4
0.4
0.2
1
1.2
1.4
1.6

Fig. 3

(b)

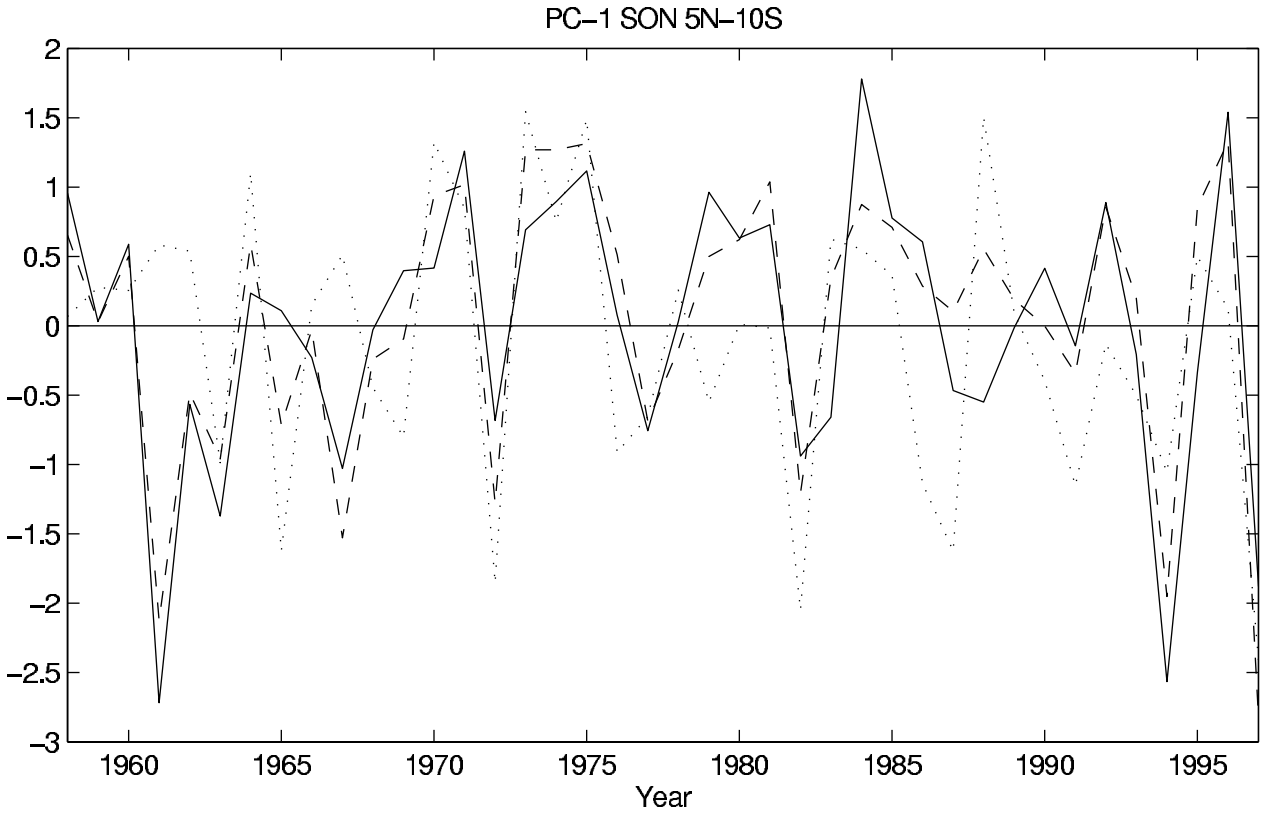
PC−1 SON 5N−10S
2
1.5
1
0.5
0
−0.5
−1
−1.5
−2
−2.5
−3
1960
1965
1970
1975
1980
1985
1990
1995
Year

Fig. 4

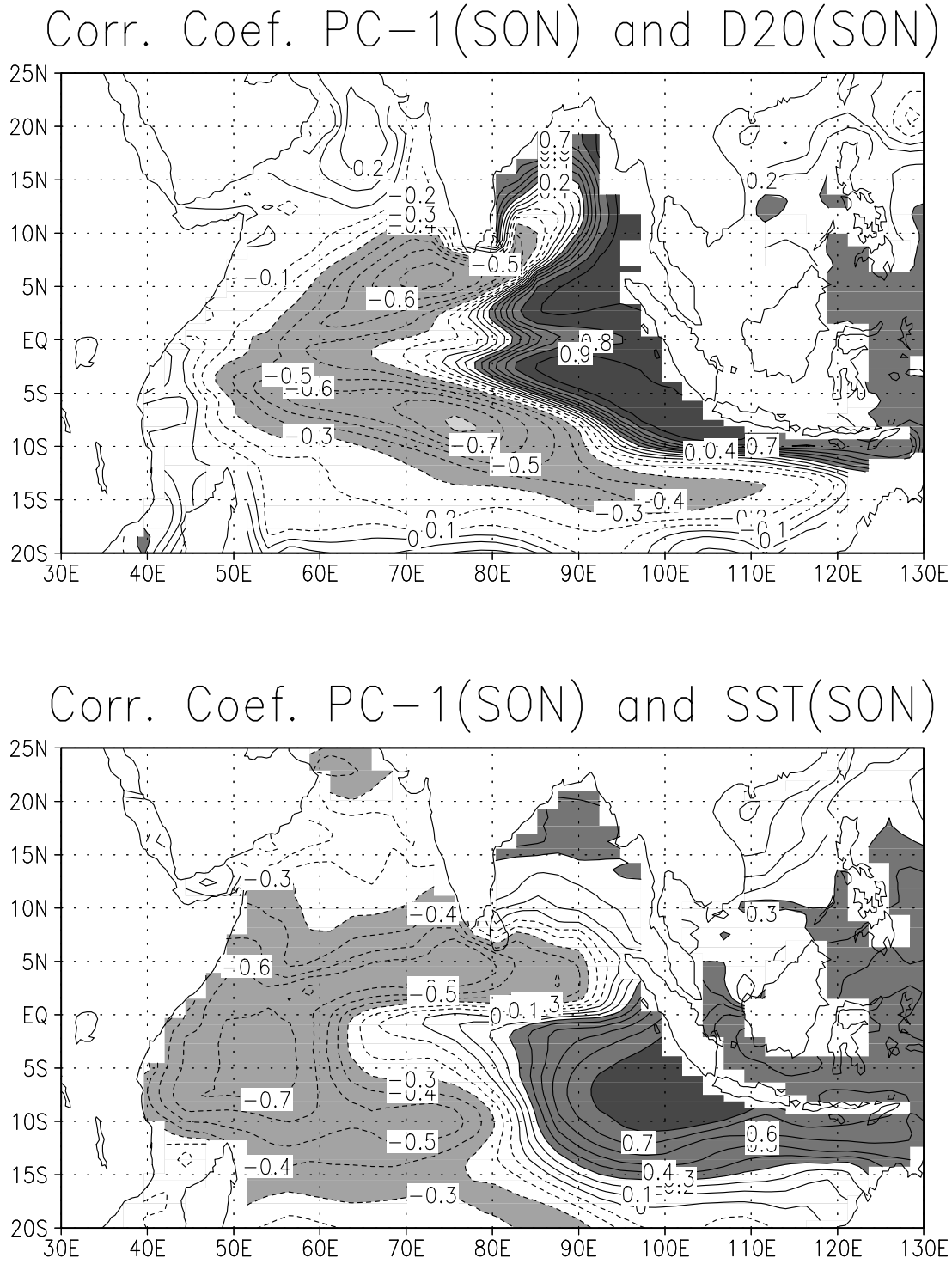
Corr. Coef. PC−1(SON) and D20(SON)
25N
20N
15N
10N
5N
EQ
5S
10S
15S
20S
30E
40E
50E
60E
70E
80E
90E
100E
110E
120E
130E
Corr. Coef. PC−1(SON) and SST(SON)

Fig. 5

(a)

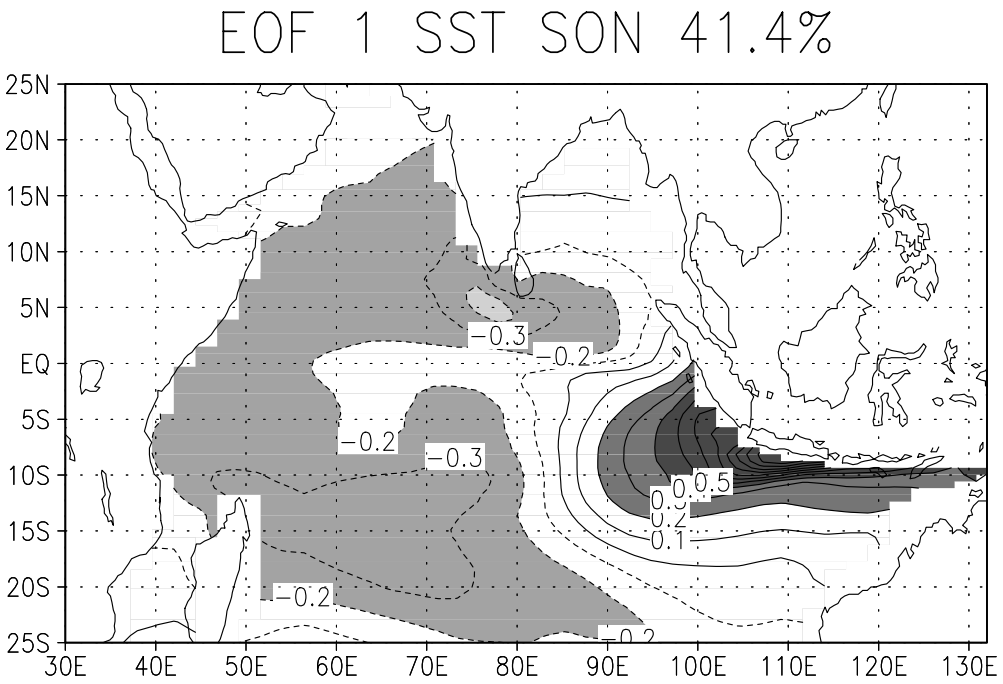
EOF 1 SST SON 41.4%
25N
20N
15N
10N
5N
EQ
5S
10S
15S
20S
25S
30E
40E
50E
60E
70E
80E
90E
100E
110E
120E
130E
−0.3
−0.2
−0.2
−0.3
0.5
0.1
−0.2
−0.2

Fig. 5

(b)

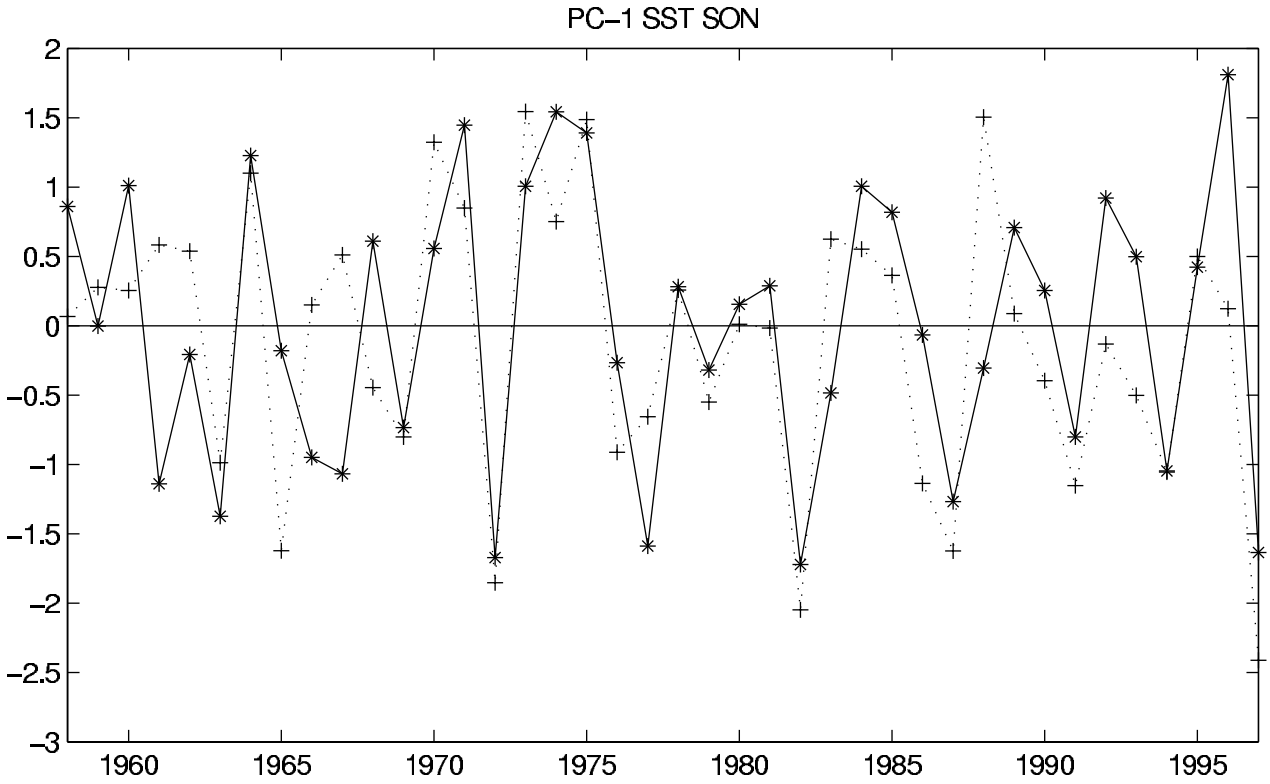
PC–1 SST SON
2
1.5
1
0.5
0
−0.5
−1
−1.5
−2
−2.5
−3
1960
1965
1970
1975
1980
1985
1990
1995

Fig. 6

(a)

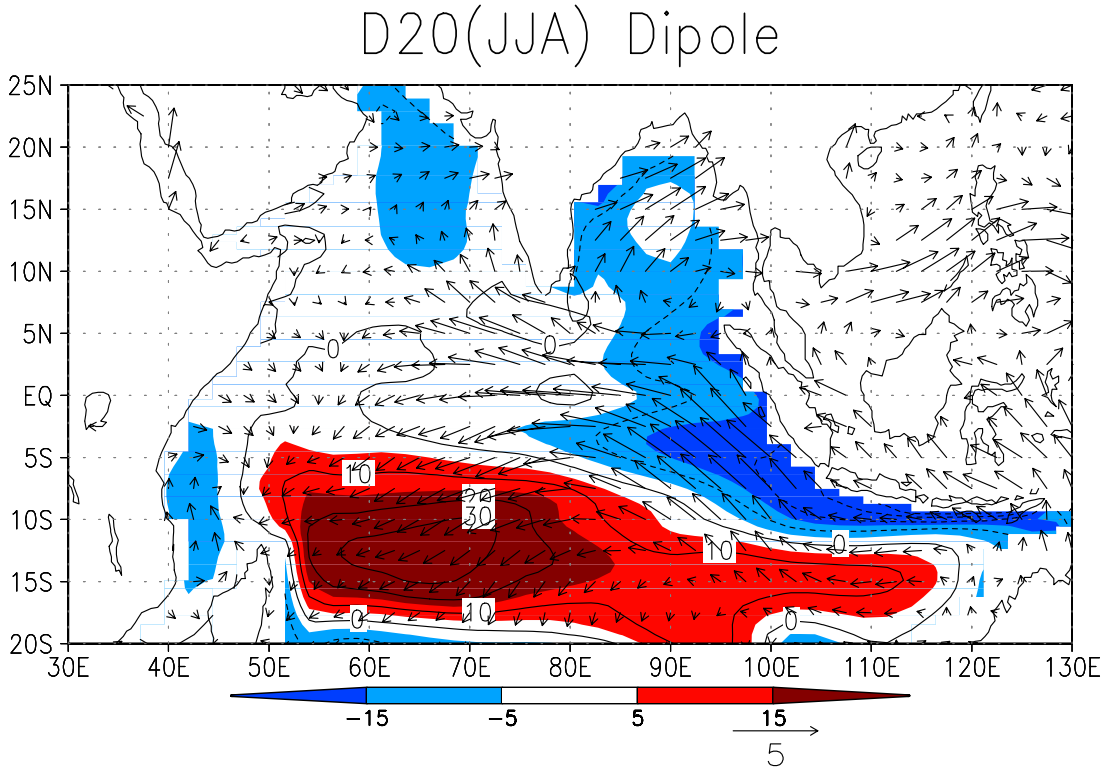
D20(JJA) Dipole
25N
20N
15N
10N
5N
EQ
5S
10S
15S
20S
30E
40E
50E
60E
70E
80E
90E
100E
110E
120E
130E
−15
−5
5
15
5

(b)

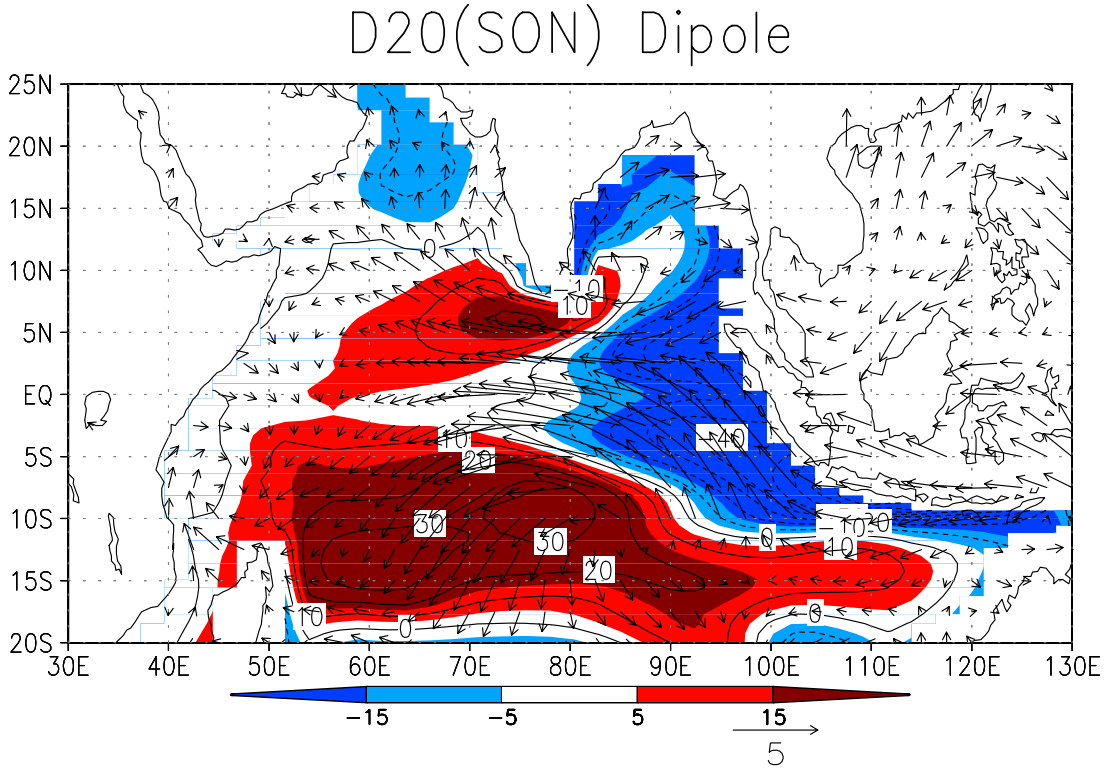
D20(SON) Dipole
25N
20N
15N
10N
5N
EQ
5S
10S
15S
20S
30E
40E
50E
60E
70E
80E
90E
100E
110E
120E
130E
−15
−5
5
15
5

Fig. 6

(c)

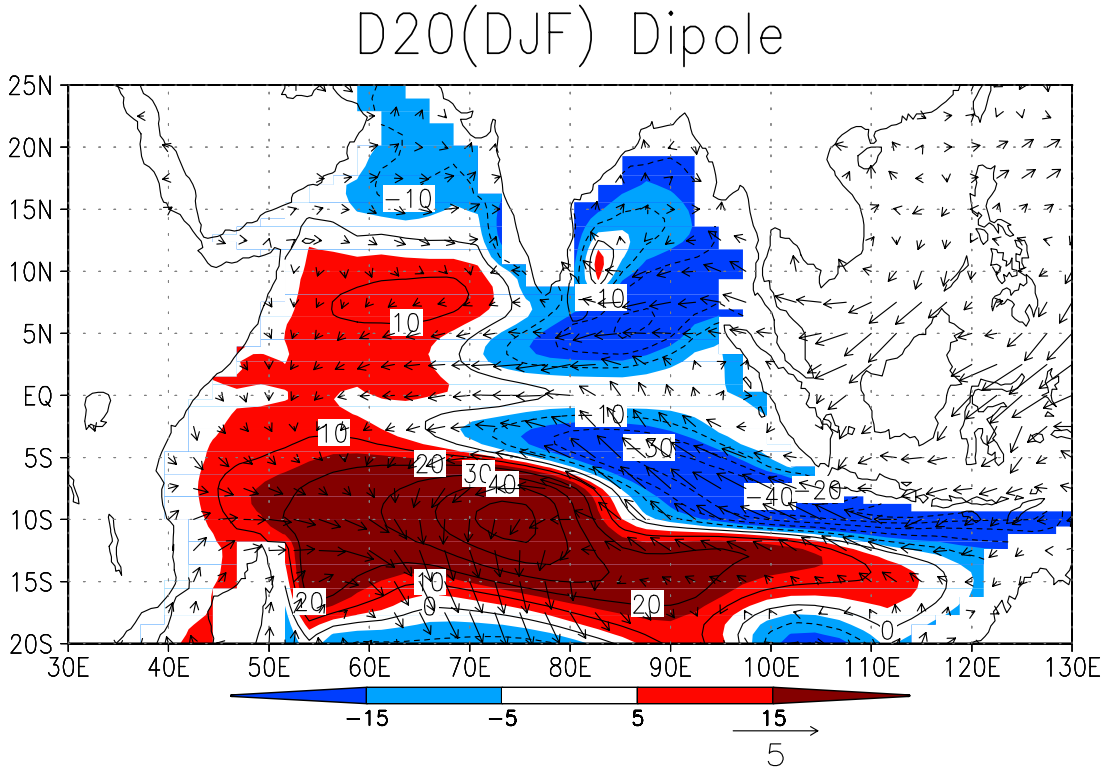
D20(DJF) Dipole
25N
20N
15N
10N
5N
EQ
5S
10S
15S
20S
30E
40E
50E
60E
70E
80E
90E
100E
110E
120E
130E
−15
−5
5
15
5

(d)

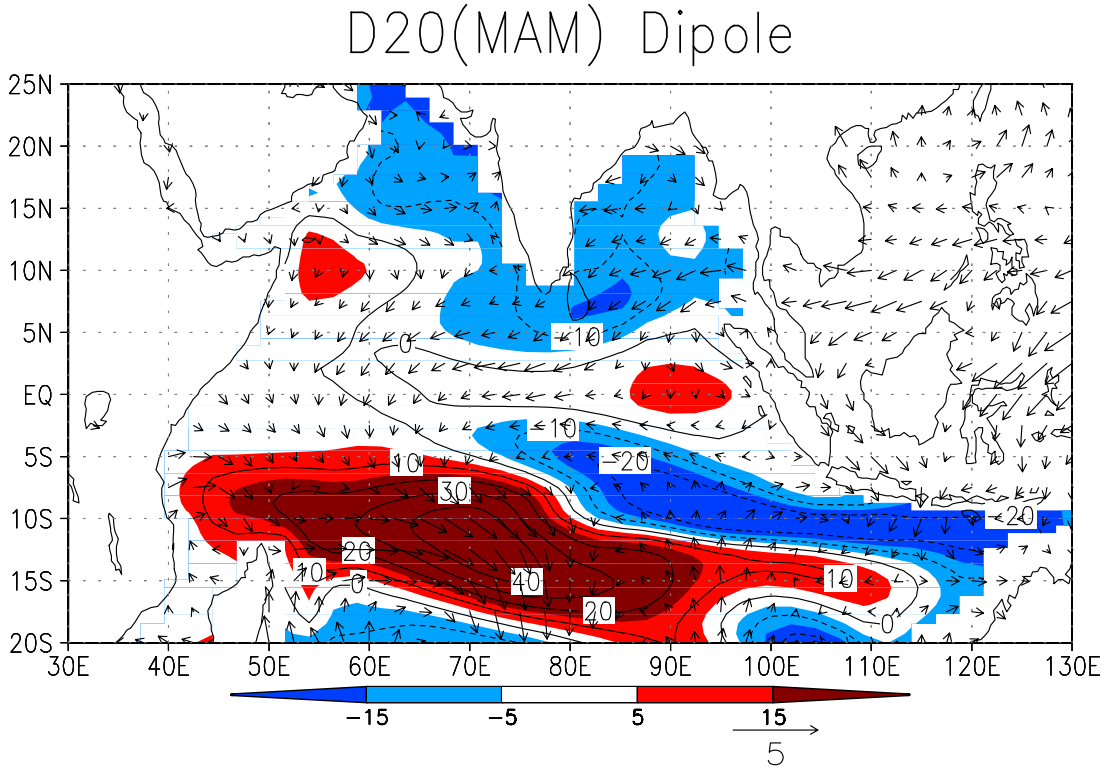
D20(MAM) Dipole
25N
20N
15N
10N
5N
EQ
5S
10S
15S
20S
30E
40E
50E
60E
70E
80E
90E
100E
110E
120E
130E
−15
−5
5
15
5

Fig. 7

(a)

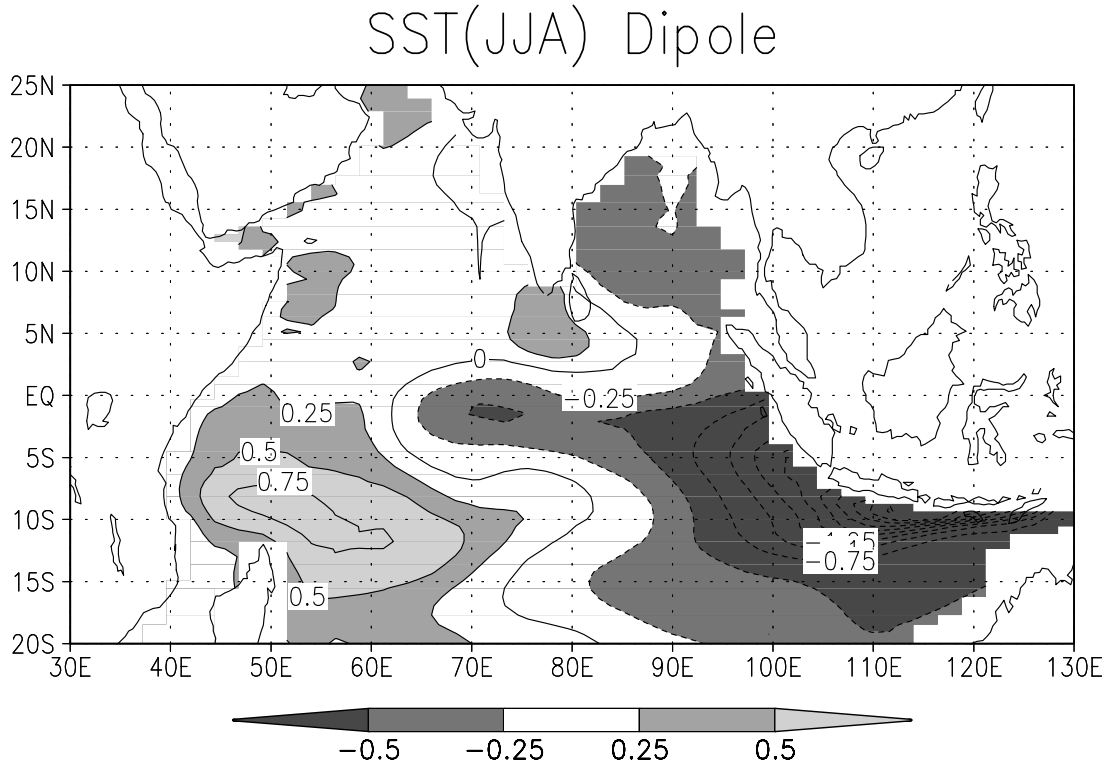
SST(JJA) Dipole
25N
20N
15N
10N
5N
EQ
5S
10S
15S
20S
30E
40E
50E
60E
70E
80E
90E
100E
110E
120E
130E
0
−0.25
0.25
0.5
0.75
0.5
−0.75
−0.5
−0.25
0.25
0.5

(b)

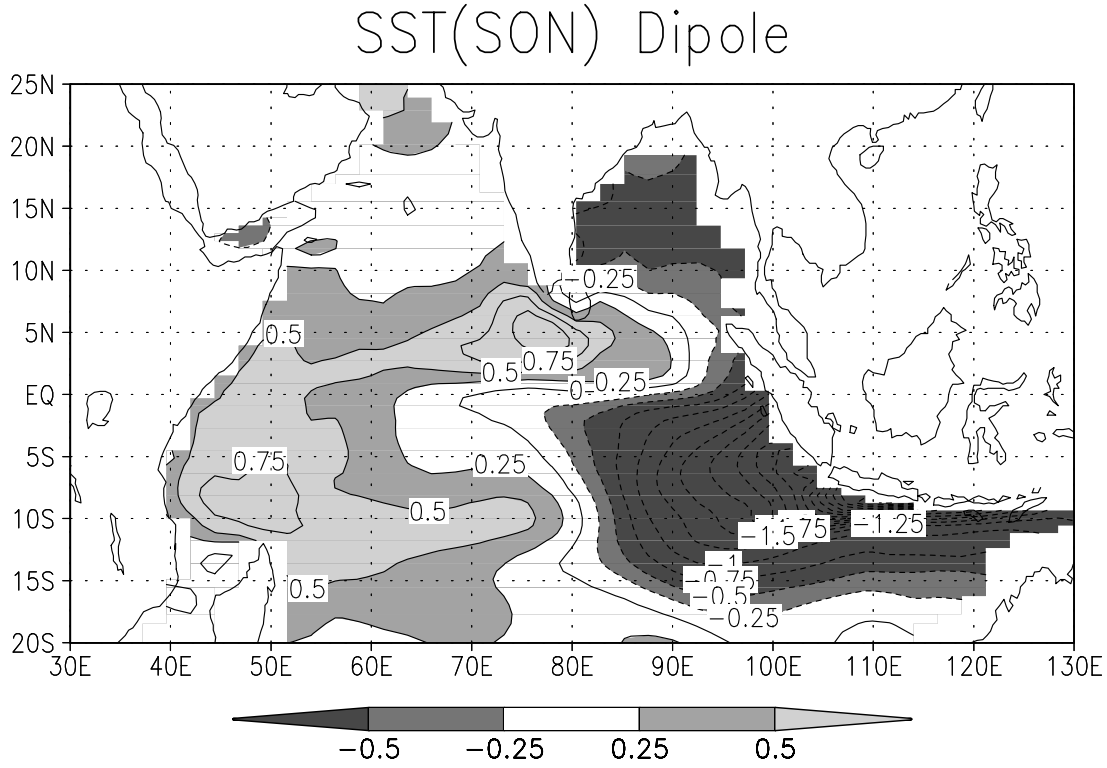
SST(SON) Dipole
25N
20N
15N
10N
5N
EQ
5S
10S
15S
20S
30E
40E
50E
60E
70E
80E
90E
100E
110E
120E
130E
−0.25
0.5
0.75
0.5
−0.25
0.75
0.25
0.5
0.5
−1.75
−1.25
−0.75
−0.5
−0.25
−0.5
−0.25
0.25
0.5

Fig. 7

(c)

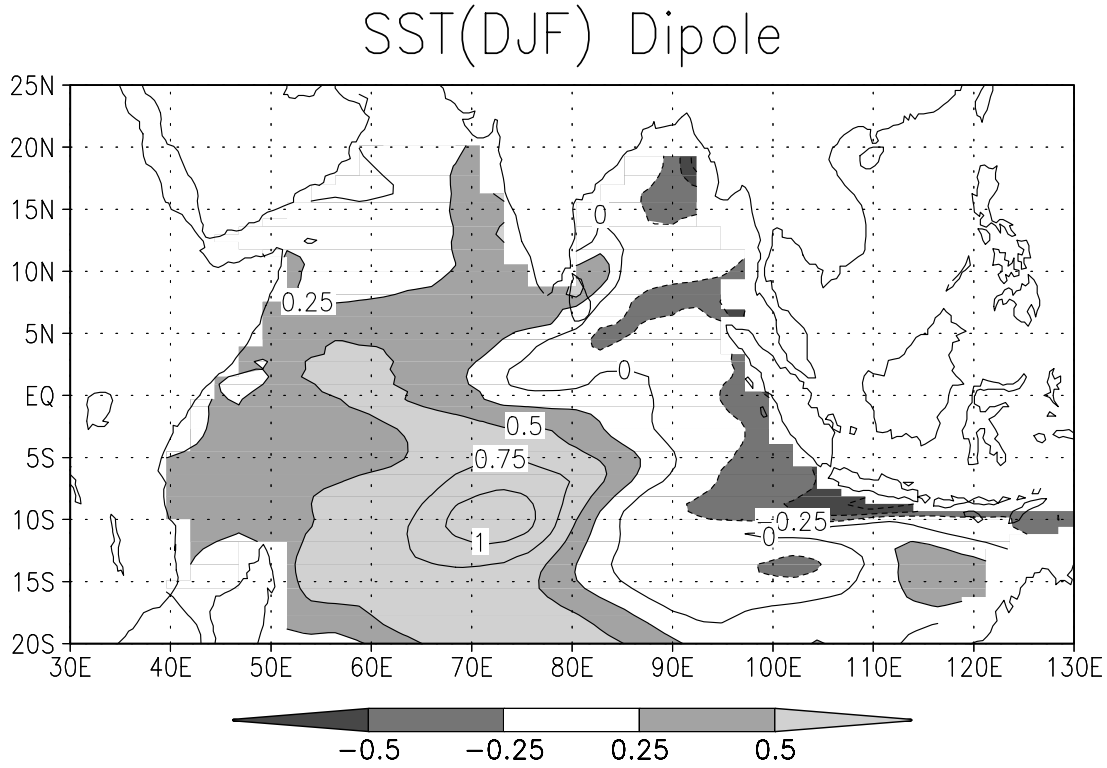
SST(DJF) Dipole
25N
20N
15N
10N
5N
EQ
5S
10S
15S
20S
30E
40E
50E
60E
70E
80E
90E
100E
110E
120E
130E
0
0.25
0
0.5
0.75
1
0.25
0
−0.5
−0.25
0.25
0.5

(d)

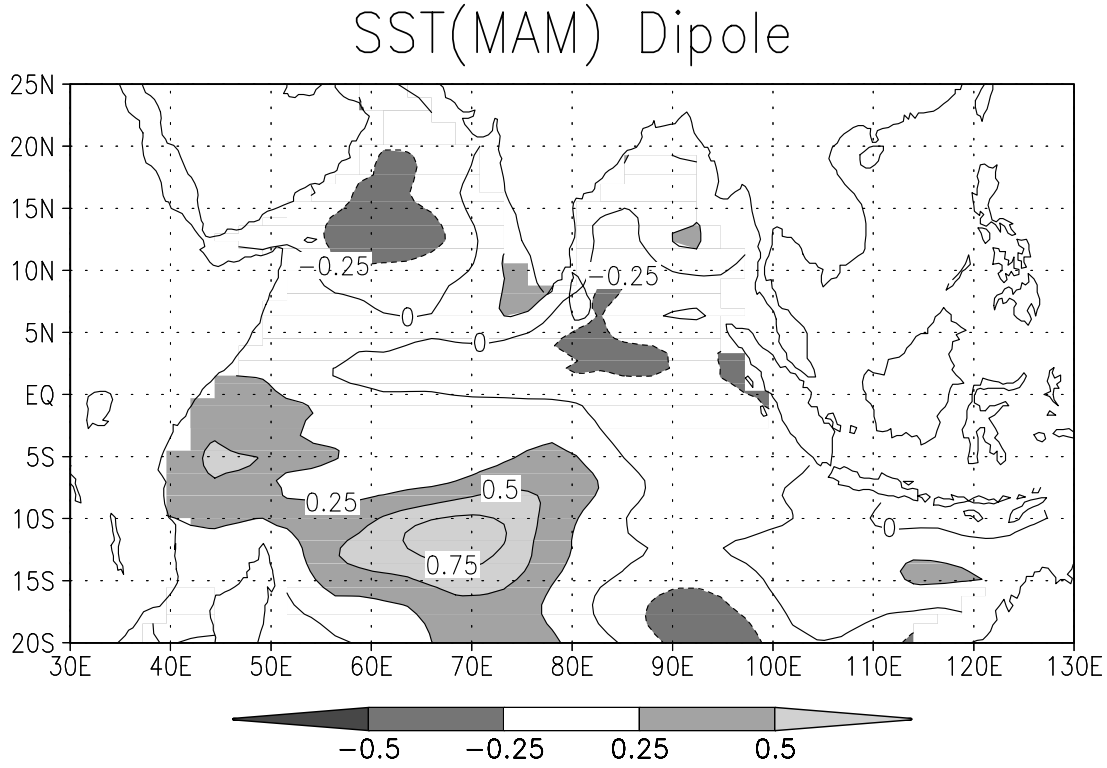
SST(MAM) Dipole
25N
20N
15N
10N
5N
EQ
5S
10S
15S
20S
30E
40E
50E
60E
70E
80E
90E
100E
110E
120E
130E
−0.25
−0.25
0
0
0.25
0.5
0.75
0
−0.5
−0.25
0.25
0.5

Fig. 8

(a)

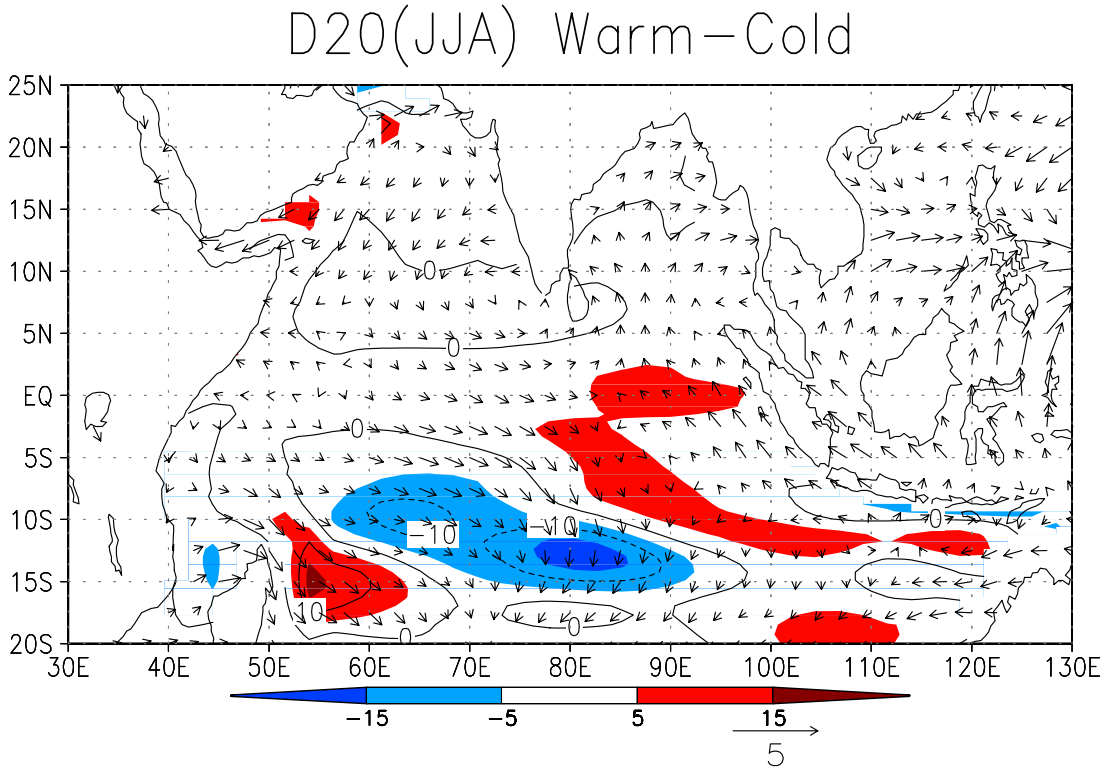
D20(JJA) Warm−Cold
25N
20N
15N
10N
5N
EQ
5S
10S
15S
20S
30E
40E
50E
60E
70E
80E
90E
100E
110E
120E
130E
−15
−5
5
15
5

(b)

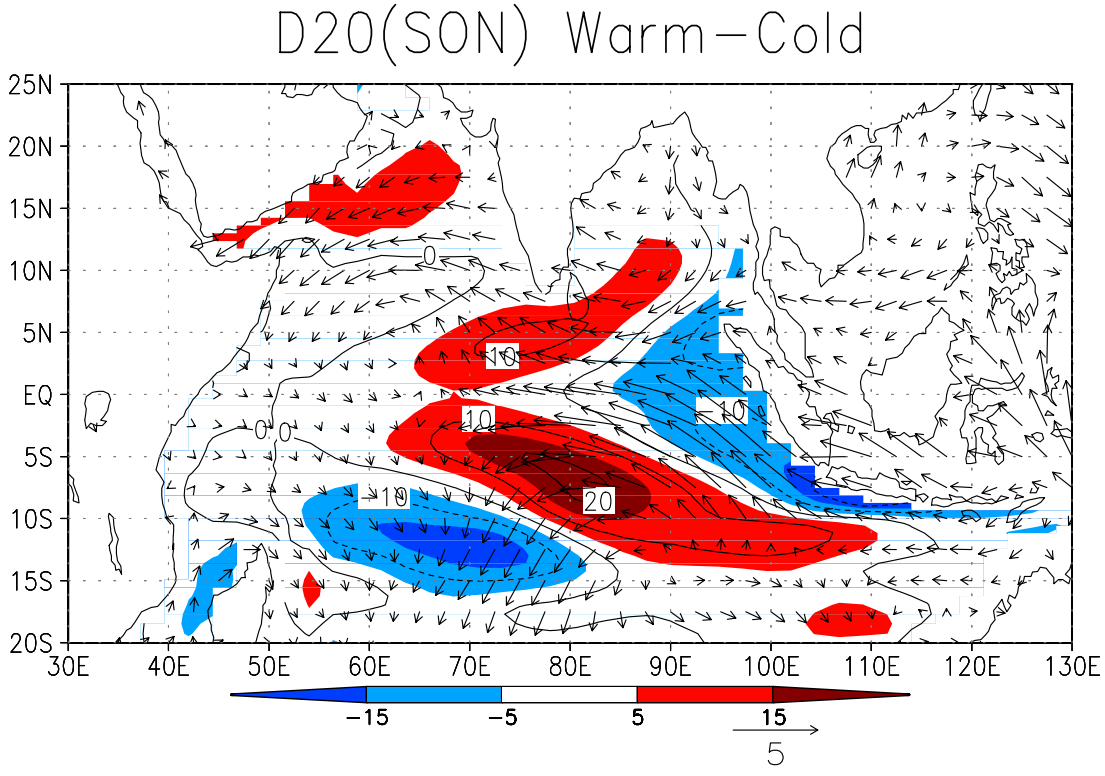
D20(SON) Warm−Cold
25N
20N
15N
10N
5N
EQ
5S
10S
15S
20S
30E
40E
50E
60E
70E
80E
90E
100E
110E
120E
130E
−15
−5
5
15
5

Fig. 8

(c)

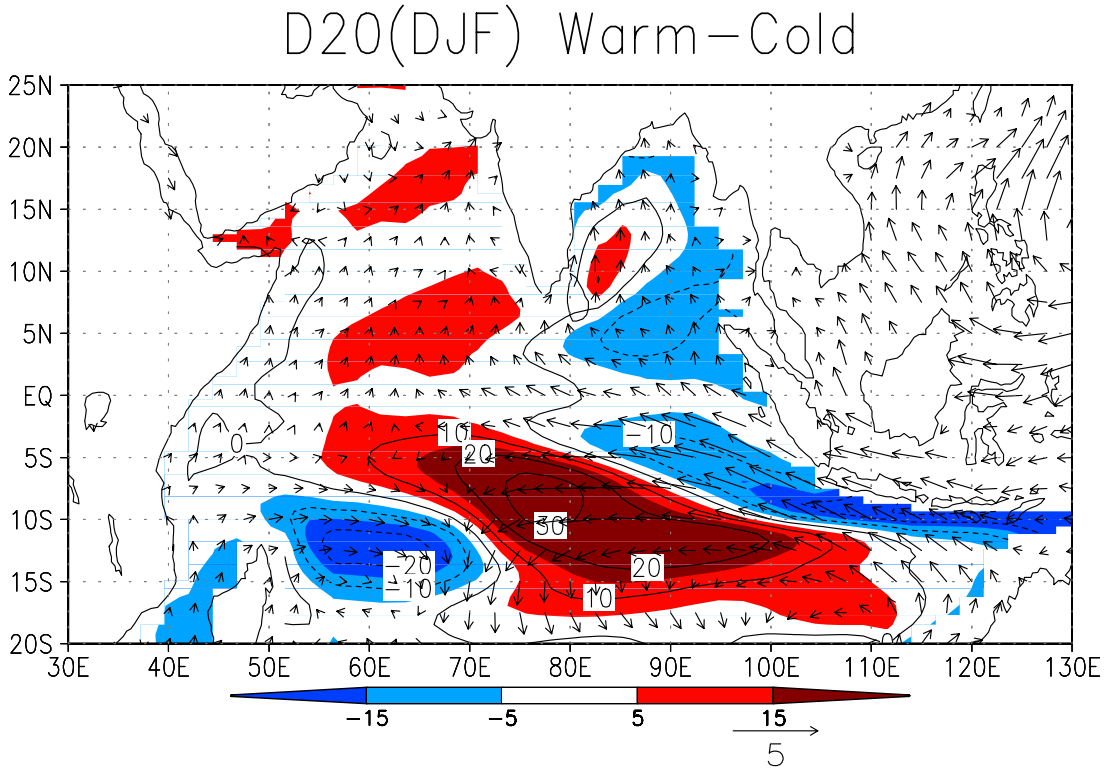
D20(DJF) Warm−Cold
25N
20N
15N
10N
5N
EQ
5S
10S
15S
20S
30E
40E
50E
60E
70E
80E
90E
100E
110E
120E
130E
−15
−5
5
15
5

(d)

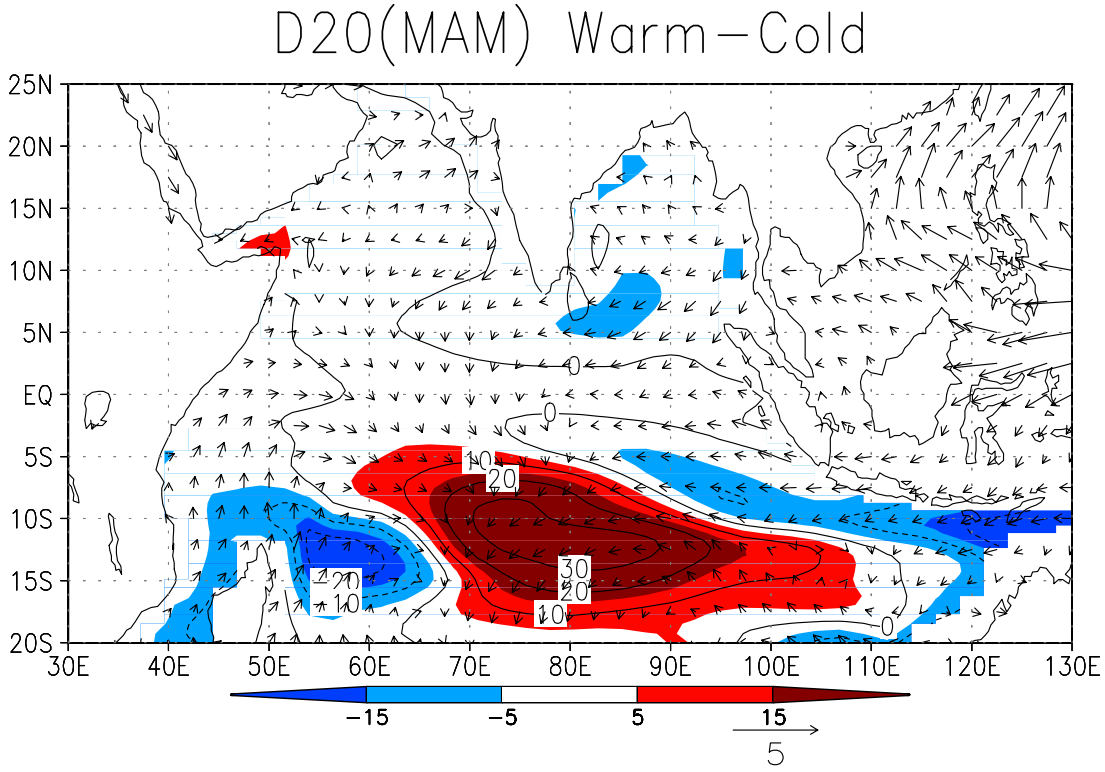
D20(MAM) Warm−Cold
25N
20N
15N
10N
5N
EQ
5S
10S
15S
20S
30E
40E
50E
60E
70E
80E
90E
100E
110E
120E
130E
−15
−5
5
15
5

Fig. 9

(a)

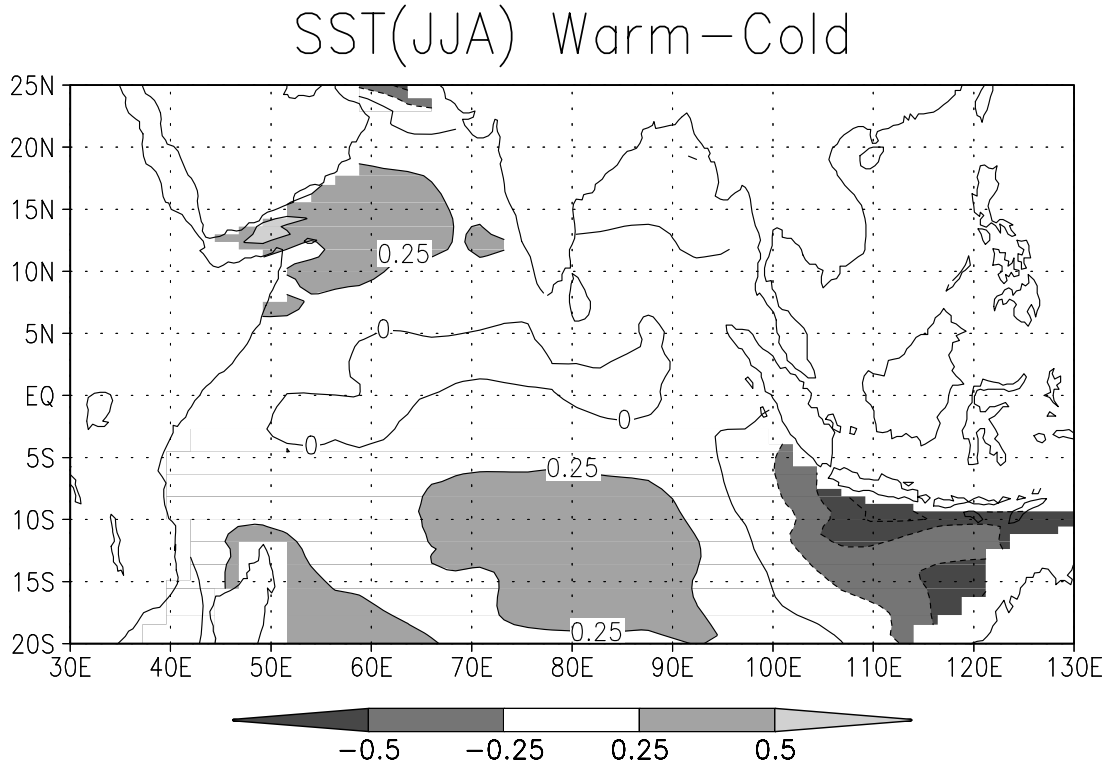
SST(JJA) Warm−Cold
25N
20N
15N
10N
5N
EQ
5S
10S
15S
20S
30E
40E
50E
60E
70E
80E
90E
100E
110E
120E
130E
0.25
0
0
0
0.25
0.25
−0.5
−0.25
0.25
0.5

(b)

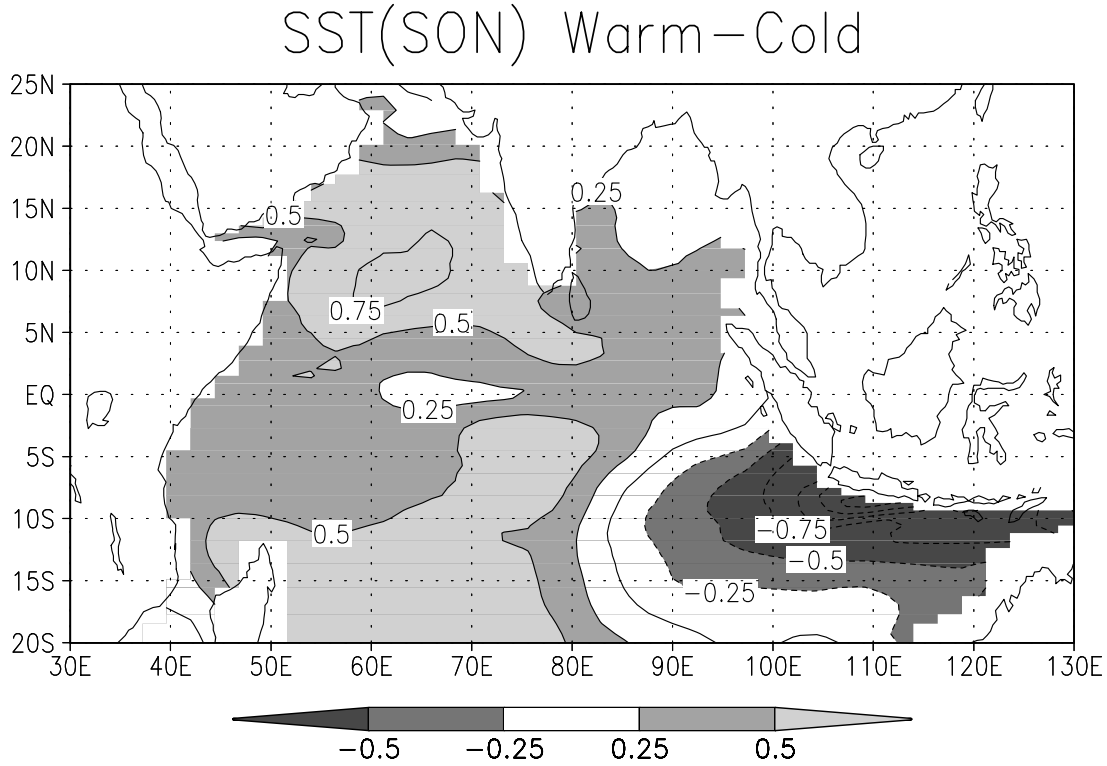
SST(SON) Warm−Cold
25N
20N
15N
10N
5N
EQ
5S
10S
15S
20S
30E
40E
50E
60E
70E
80E
90E
100E
110E
120E
130E
0.5
0.25
0.75
0.5
0.25
0.5
−0.75
−0.5
−0.25
−0.5
−0.25
0.25
0.5

Fig. 9

(c)

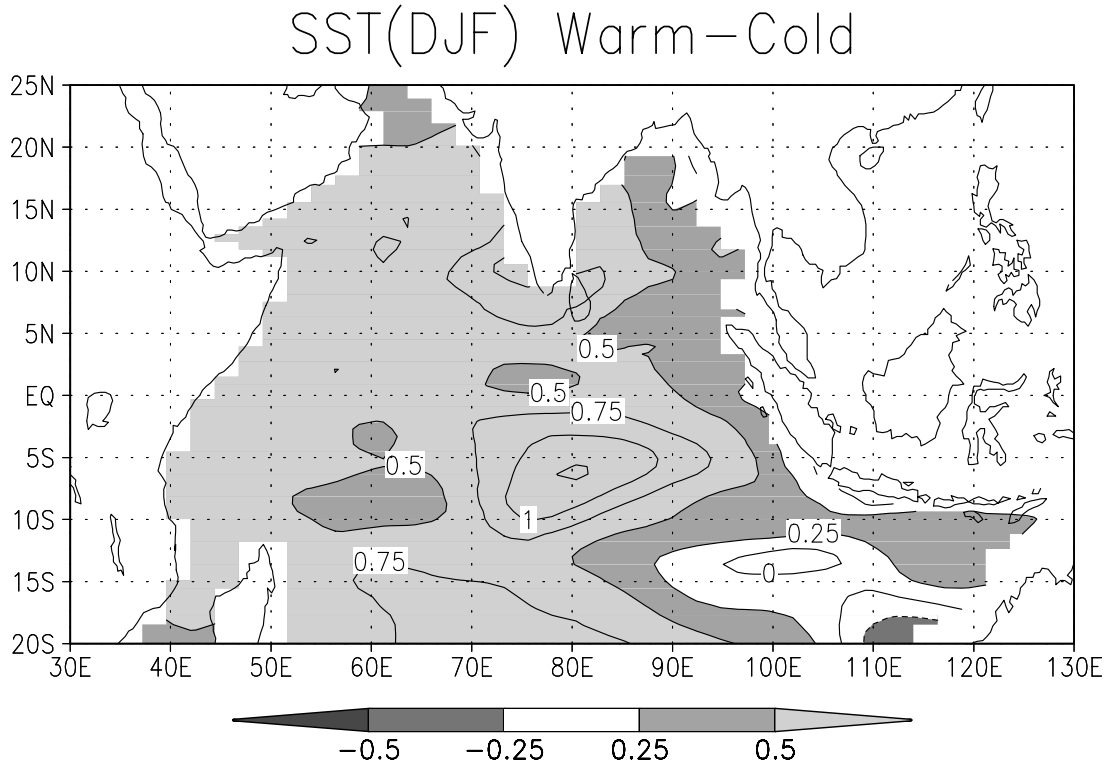
SST(DJF) Warm−Cold
25N
20N
15N
10N
5N
EQ
5S
10S
15S
20S
30E
40E
50E
60E
70E
80E
90E
100E
110E
120E
130E
0.5
0.5
0.75
0.5
1
0.75
0.25
0
−0.5
−0.25
0.25
0.5

(d)

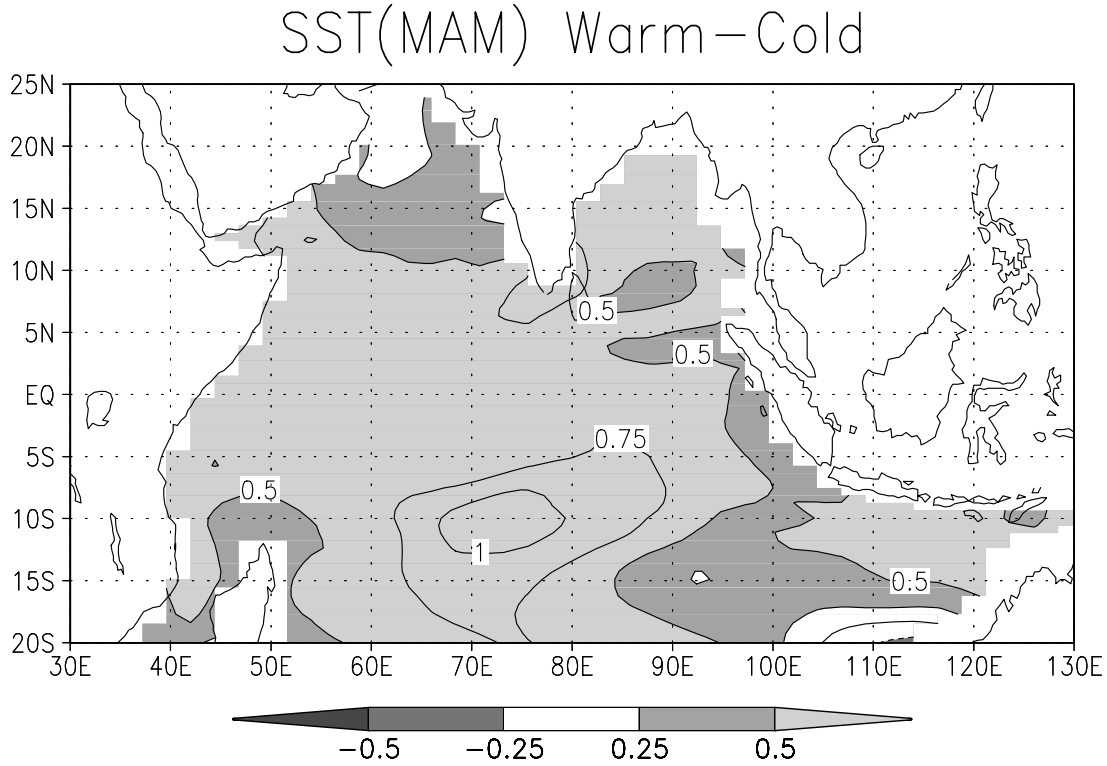
SST(MAM) Warm−Cold
25N
20N
15N
10N
5N
EQ
5S
10S
15S
20S
30E
40E
50E
60E
70E
80E
90E
100E
110E
120E
130E
0.5
0.5
0.75
0.5
1
0.5
−0.5
−0.25
0.25
0.5

Fig. 10

(a)

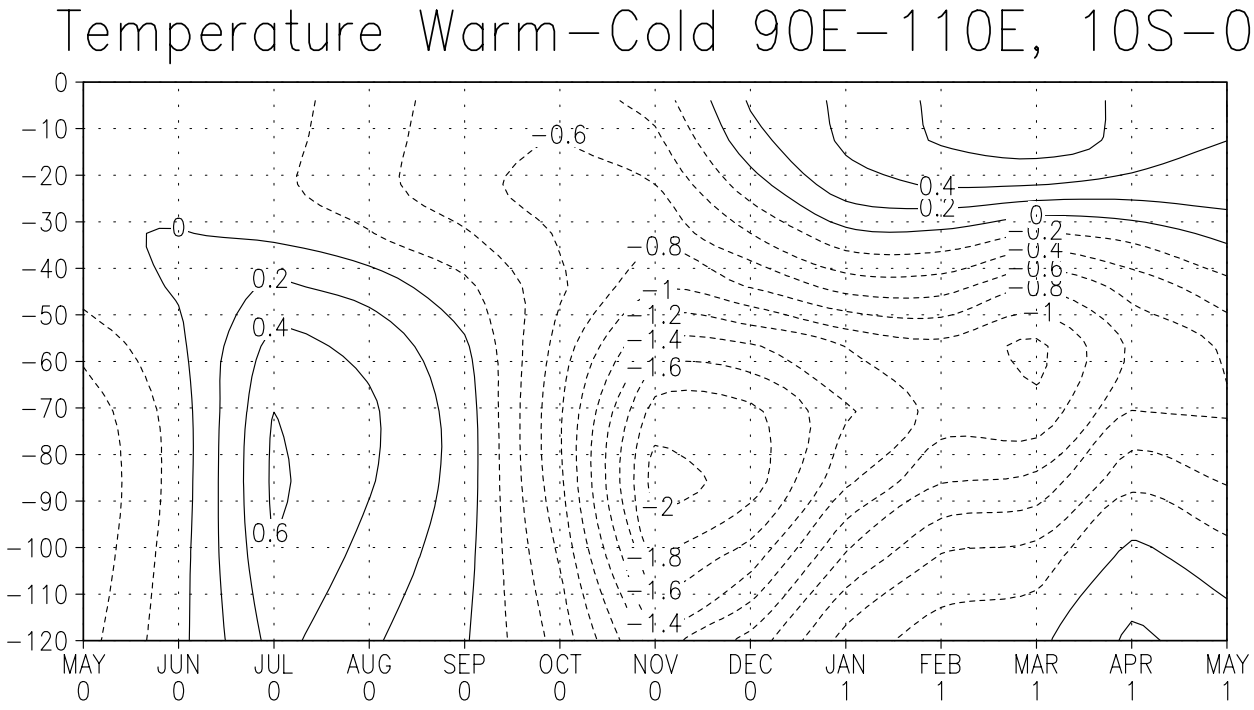
Temperature Warm−Cold 90E−110E, 10S−0
0
−10
−20
−30
−40
−50
−60
−70
−80
−90
−100
−110
−120
MAY 0
JUN 0
JUL 0
AUG 0
SEP 0
OCT 0
NOV 0
DEC 0
JAN 1
FEB 1
MAR 1
APR 1
MAY 1

(b)

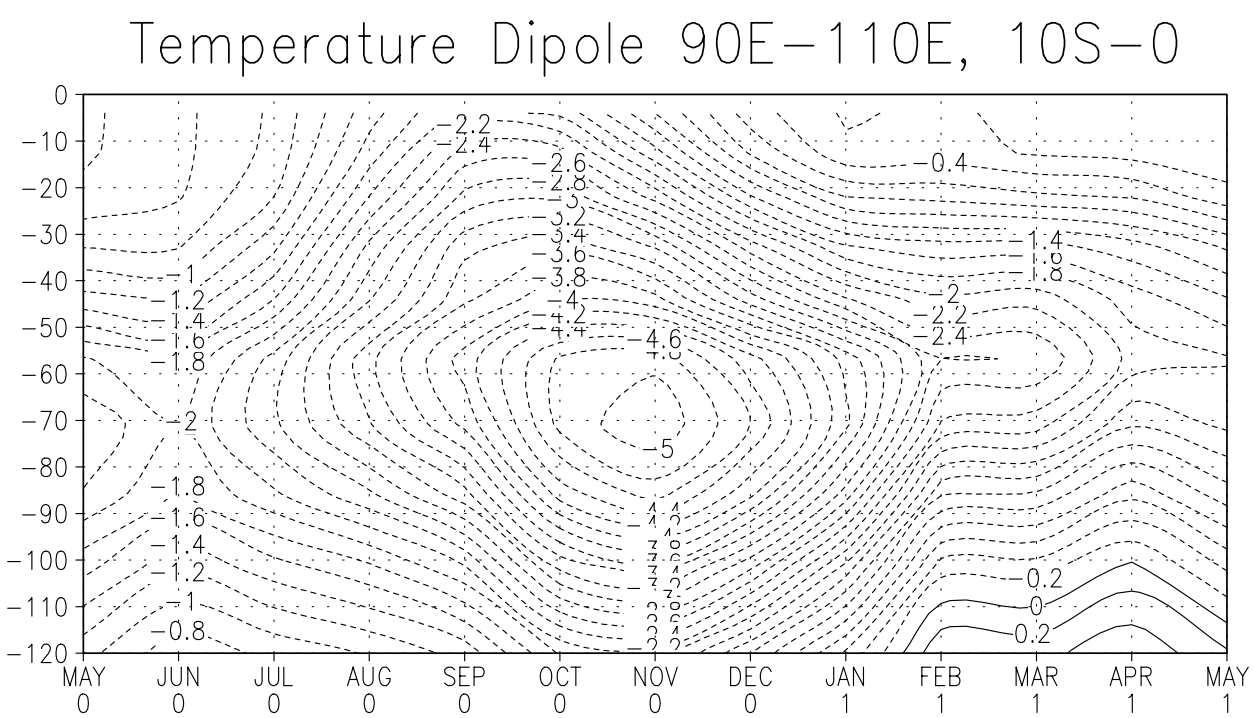
Temperature Dipole 90E−110E, 10S−0
0
−10
−20
−30
−40
−50
−60
−70
−80
−90
−100
−110
−120
MAY 0
JUN 0
JUL 0
AUG 0
SEP 0
OCT 0
NOV 0
DEC 0
JAN 1
FEB 1
MAR 1
APR 1
MAY 1

Fig. 11

(a)

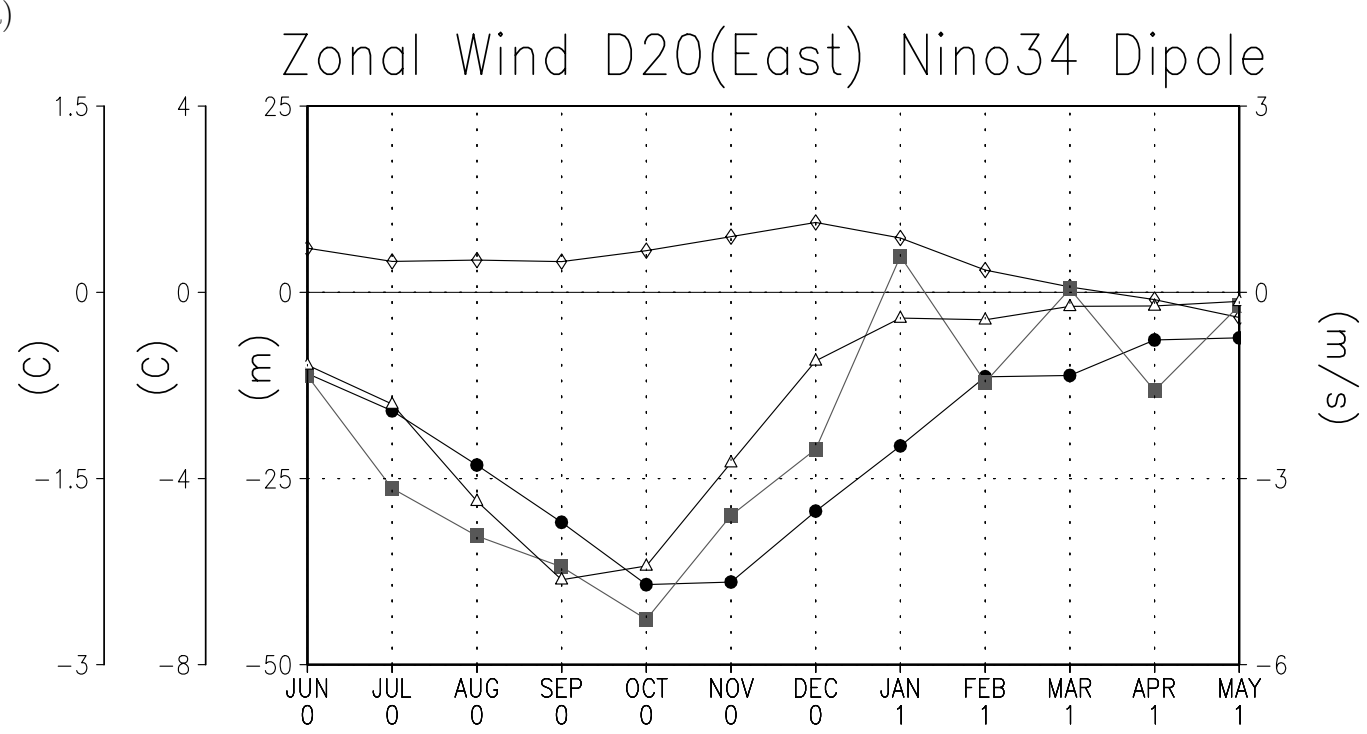
Zonal Wind D20(East) Nino34 Dipole
1.5
0
−1.5
−3
(C)
4
0
−4
−8
(C)
25
0
−25
−50
(m)
3
0
−3
−6
(s/m)
JUN 0
JUL 0
AUG 0
SEP 0
OCT 0
NOV 0
DEC 0
JAN 1
FEB 1
MAR 1
APR 1
MAY 1

(b)

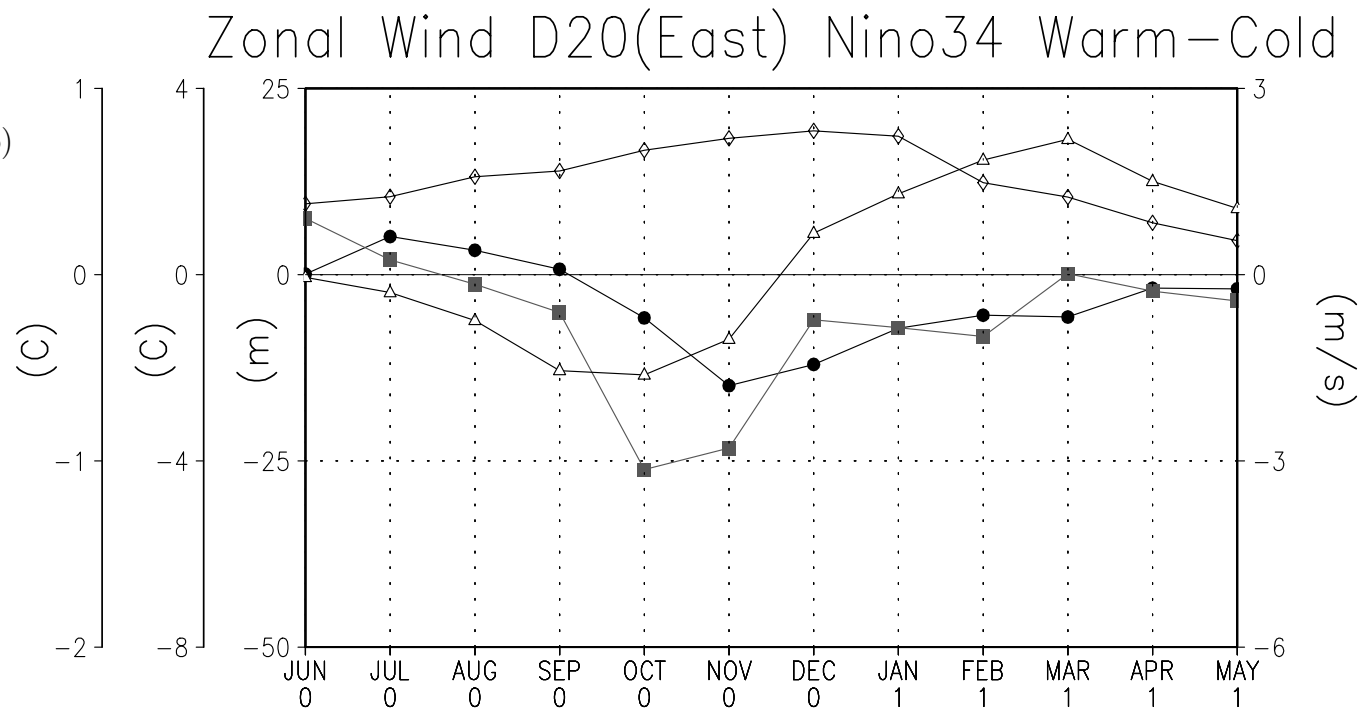
Zonal Wind D20(East) Nino34 Warm−Cold
1
0
−1
−2
(C)
4
0
−4
−8
(C)
25
0
−25
−50
(m)
3
0
−3
−6
(s/m)
JUN 0
JUL 0
AUG 0
SEP 0
OCT 0
NOV 0
DEC 0
JAN 1
FEB 1
MAR 1
APR 1
MAY 1

Fig. 12

(a)

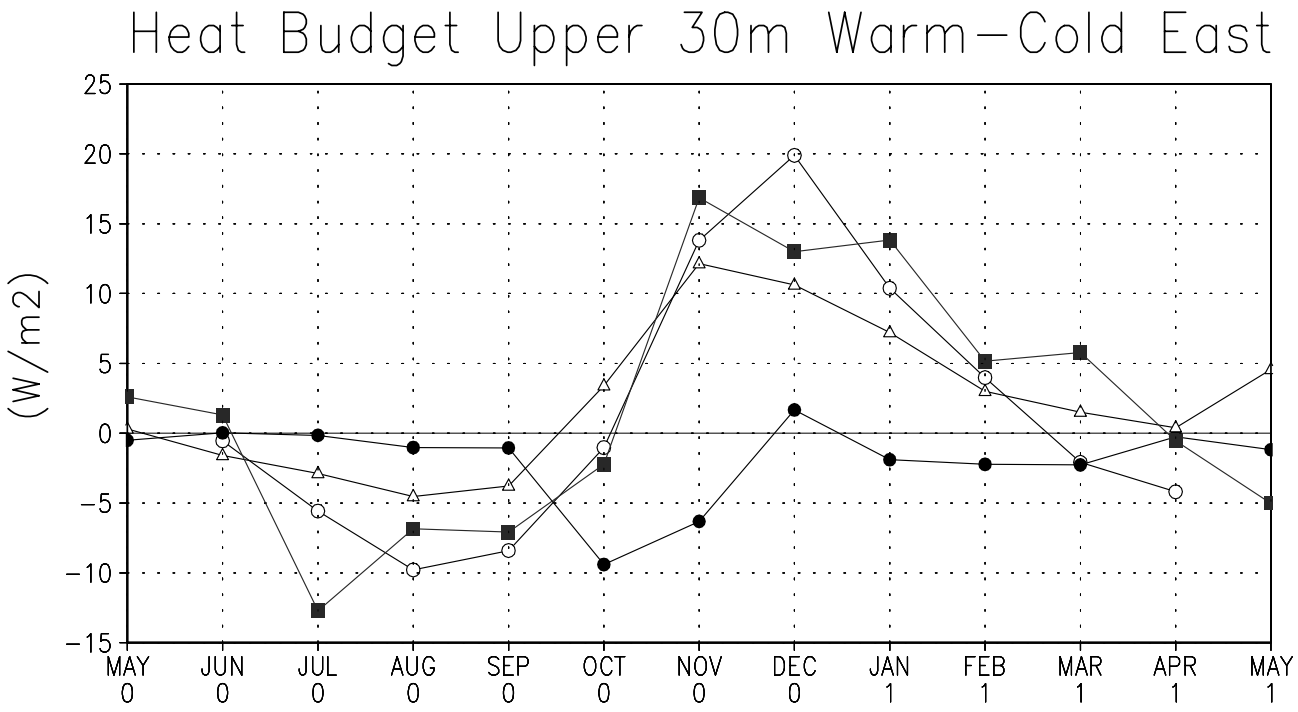
Heat Budget Upper 30m Warm−Cold East
(W/m2)
25
20
15
10
5
0
−5
−10
−15
MAY 0
JUN 0
JUL 0
AUG 0
SEP 0
OCT 0
NOV 0
DEC 0
JAN 1
FEB 1
MAR 1
APR 1
MAY 1

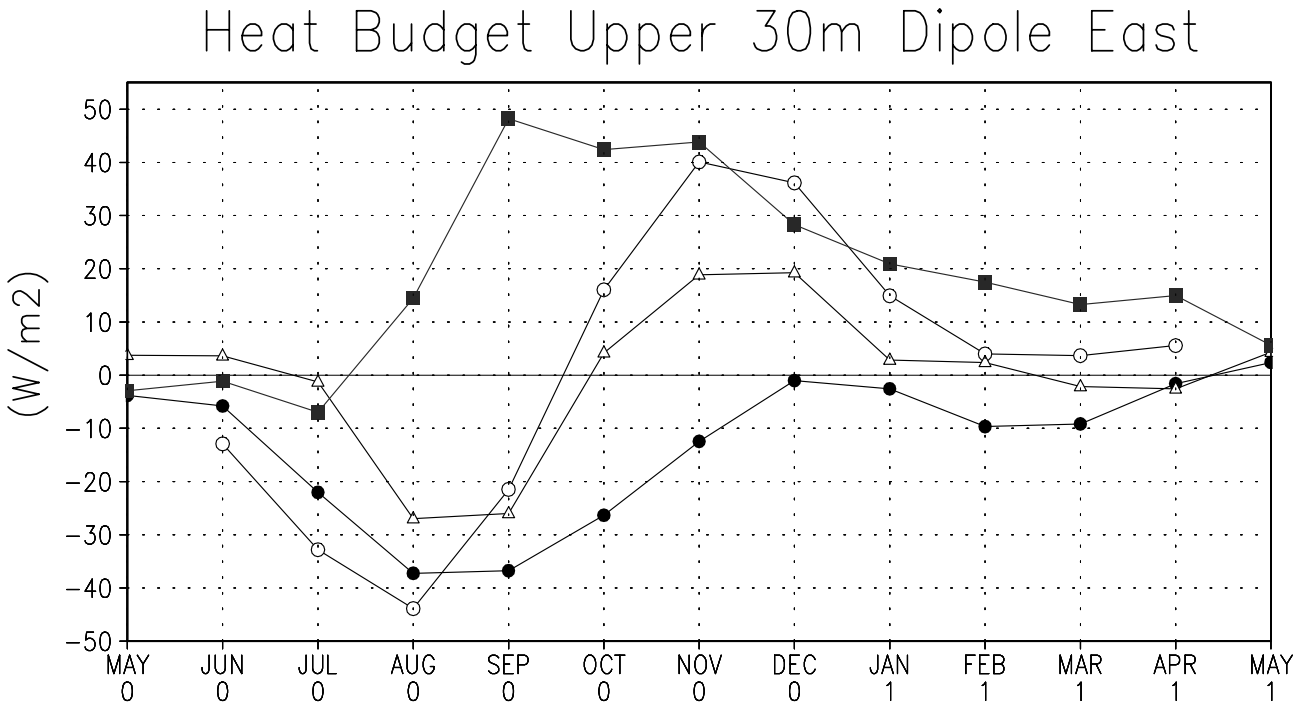
Heat Budget Upper 30m Dipole East
(W/m2)
50
40
30
20
10
0
−10
−20
−30
−40
−50
MAY 0
JUN 0
JUL 0
AUG 0
SEP 0
OCT 0
NOV 0
DEC 0
JAN 1
FEB 1
MAR 1
APR 1
MAY 1

Fig. 12

(b)

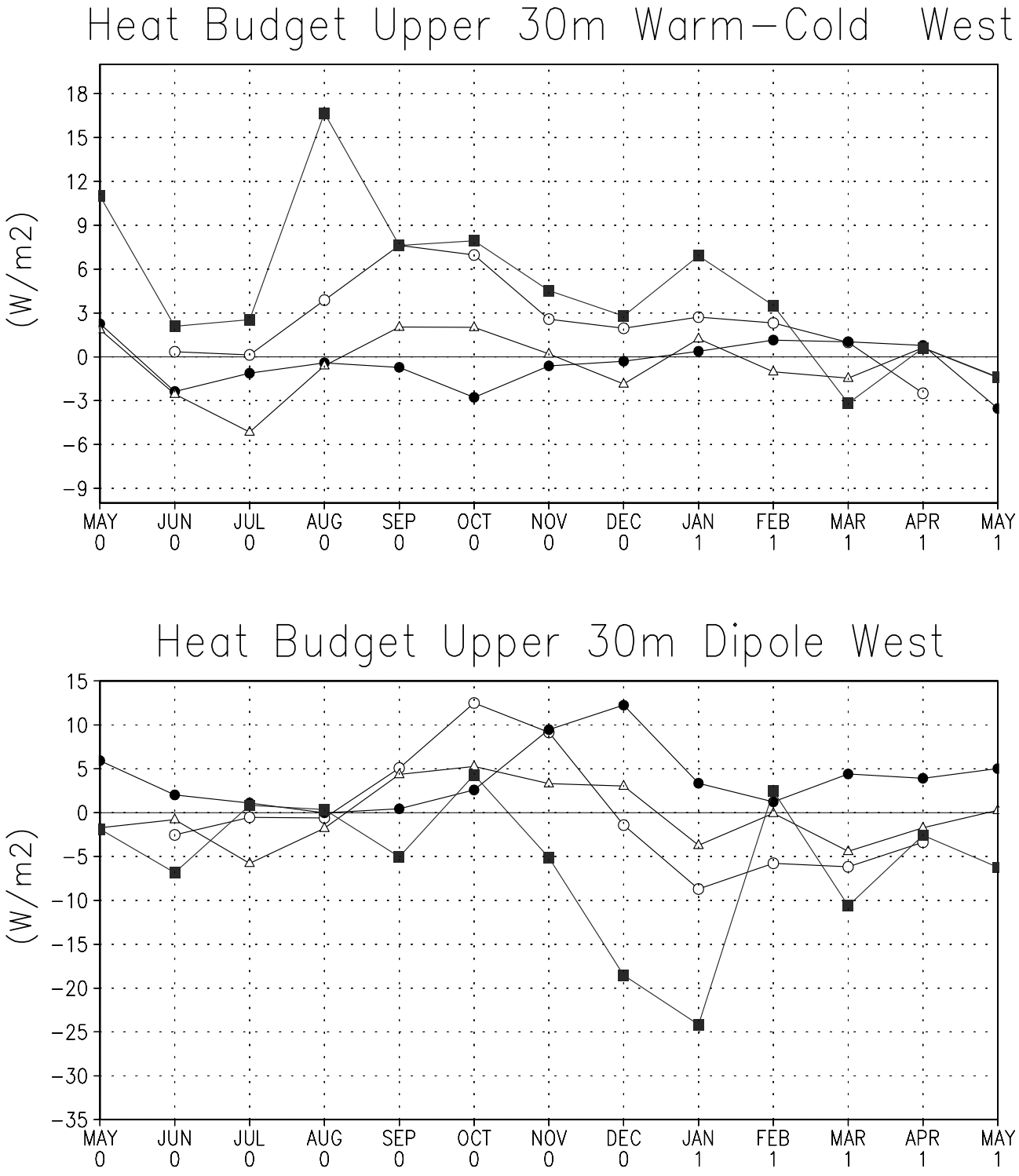
Heat Budget Upper 30m Warm−Cold West
(W/m2)
18
15
12
9
6
3
0
−3
−6
−9
MAY 0
JUN 0
JUL 0
AUG 0
SEP 0
OCT 0
NOV 0
DEC 0
JAN 1
FEB 1
MAR 1
APR 1
MAY 1
Heat Budget Upper 30m Dipole West
(W/m2)
15
10
5
0
−5
−10
−15
−20
−25
−30
−35
MAY 0
JUN 0
JUL 0
AUG 0
SEP 0
OCT 0
NOV 0
DEC 0
JAN 1
FEB 1
MAR 1
APR 1
MAY 1

Fig. 13

(a)

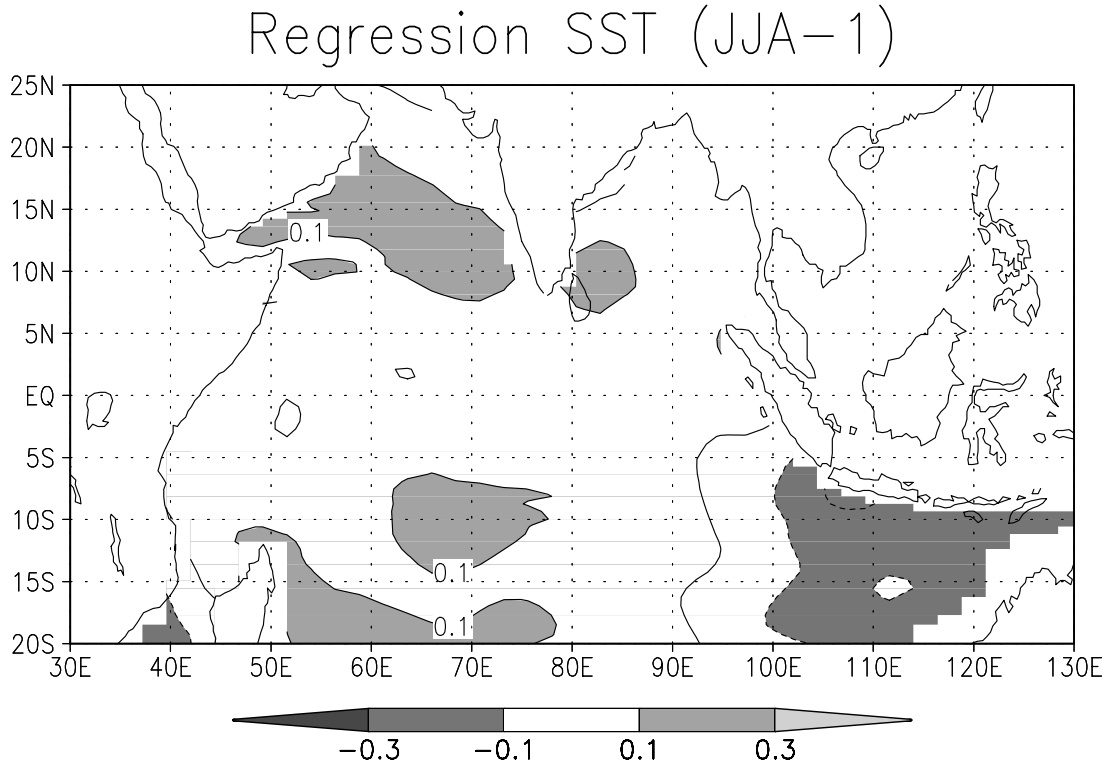
Regression SST (JJA−1)
25N
20N
15N
10N
5N
EQ
5S
10S
15S
20S
30E
40E
50E
60E
70E
80E
90E
100E
110E
120E
130E
0.1
0.1
0.1
−0.3
−0.1
0.1
0.3

(b)

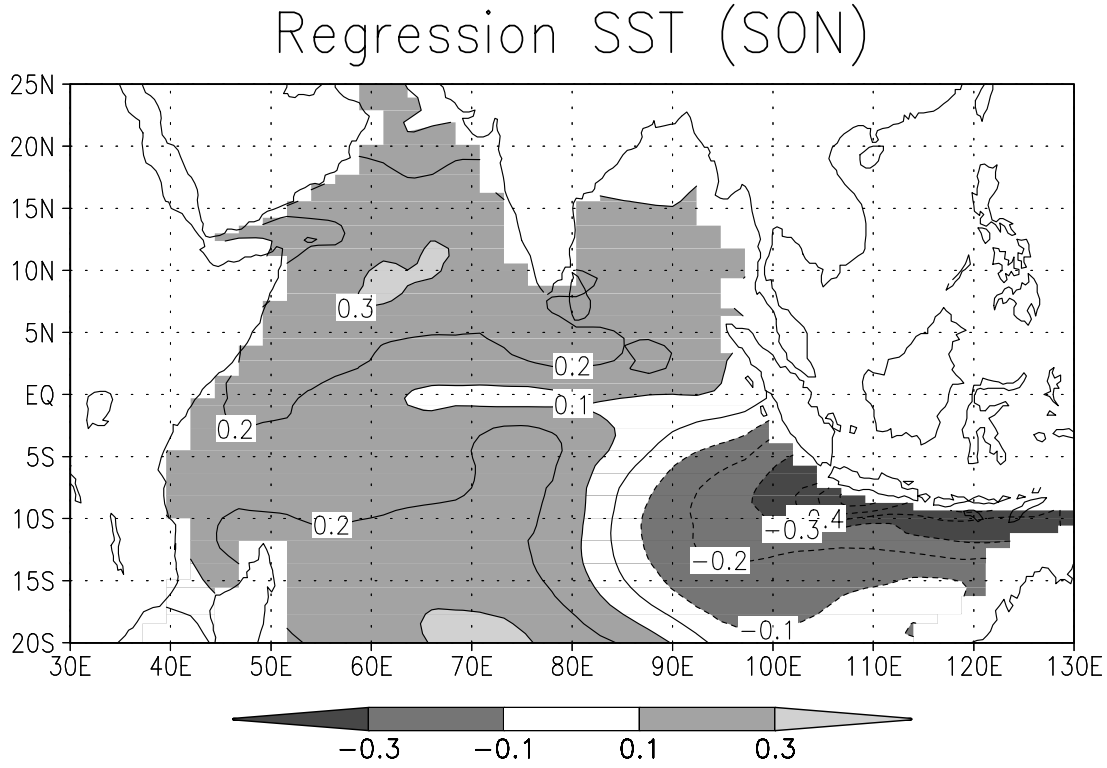
Regression SST (SON)
25N
20N
15N
10N
5N
EQ
5S
10S
15S
20S
30E
40E
50E
60E
70E
80E
90E
100E
110E
120E
130E
0.3
0.2
0.1
0.2
0.2
−0.3
−0.4
−0.2
−0.1
−0.3
−0.1
0.1
0.3

Fig. 13

(c)

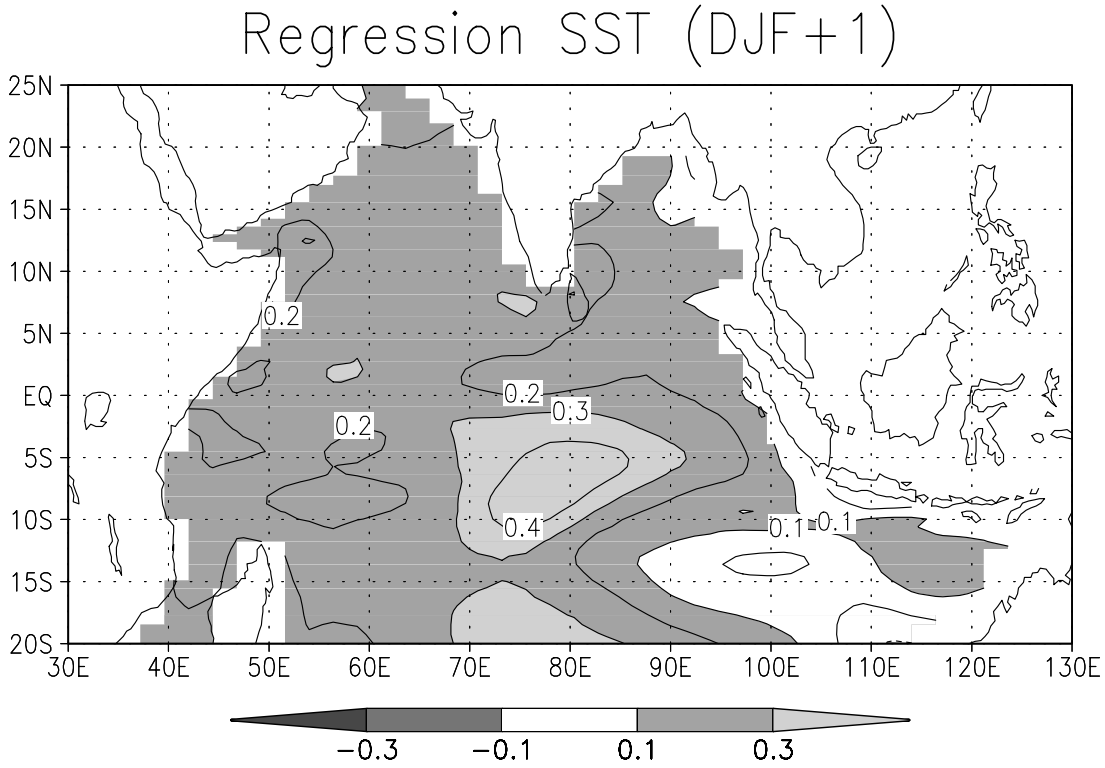
Regression SST (DJF+1)
25N
20N
15N
10N
5N
EQ
5S
10S
15S
20S
30E
40E
50E
60E
70E
80E
90E
100E
110E
120E
130E
0.2
0.2
0.2
0.3
0.4
0.1
0.1
−0.3
−0.1
0.1
0.3

Fig. 14

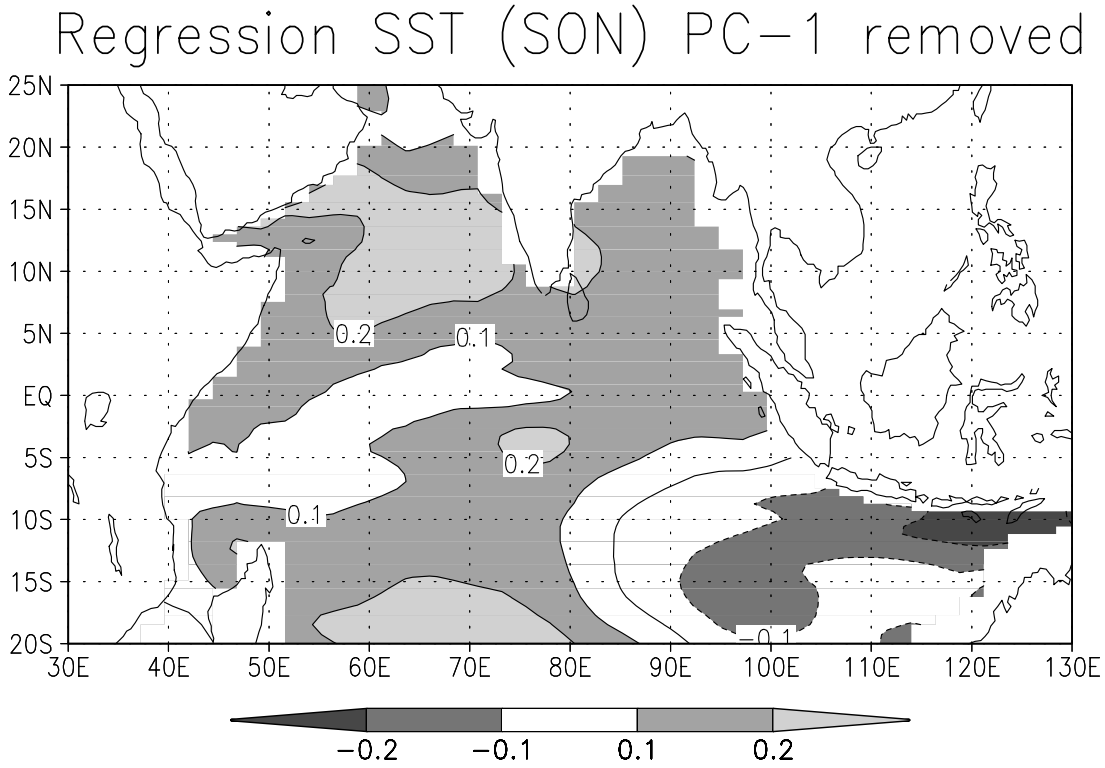
Regression SST (SON) PC−1 removed
25N
20N
15N
10N
5N
EQ
5S
10S
15S
20S
30E
40E
50E
60E
70E
80E
90E
100E
110E
120E
130E
0.2
0.1
0.2
0.1
−0.1
−0.2
−0.1
0.1
0.2

Fig. 15

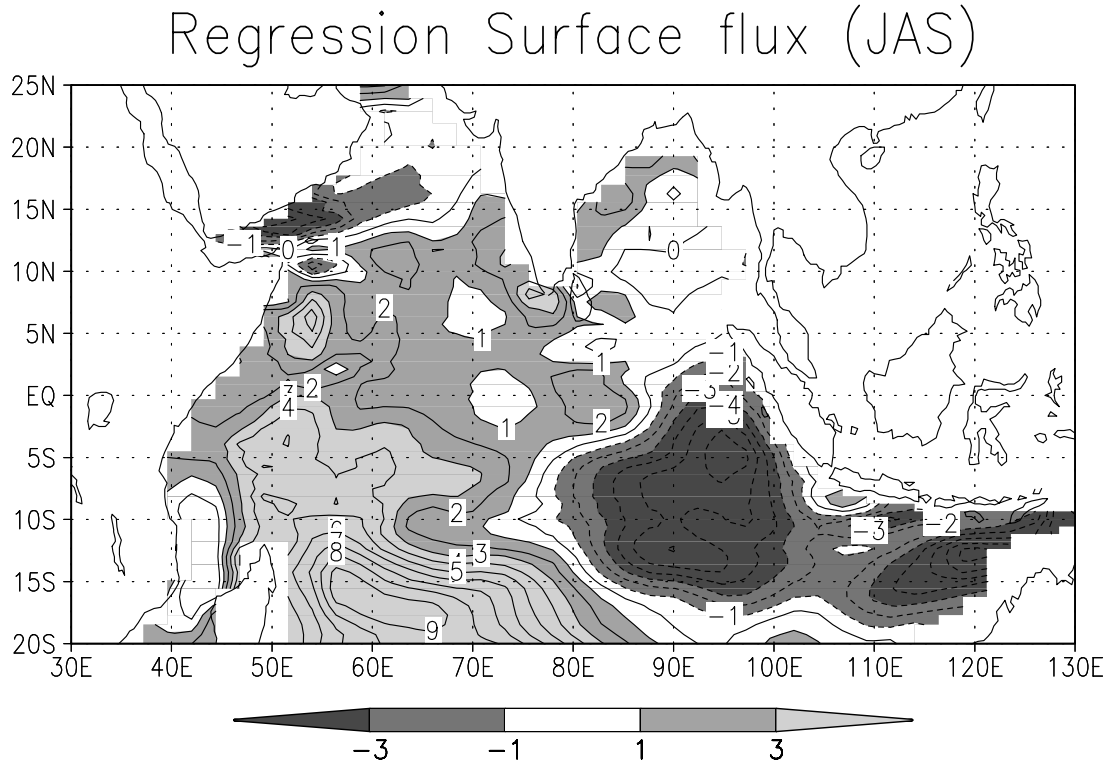
Regression Surface flux (JAS)
25N
20N
15N
10N
5N
EQ
5S
10S
15S
20S
30E
40E
50E
60E
70E
80E
90E
100E
110E
120E
130E
−3
−1
1
3

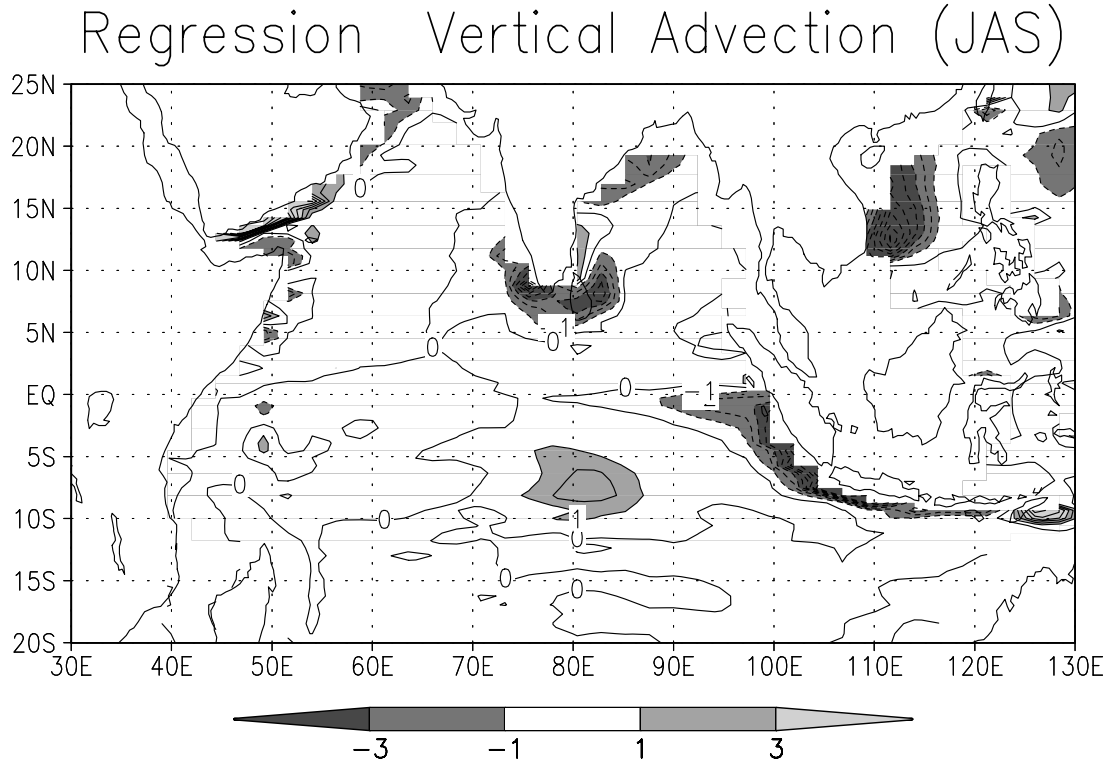
Regression Vertical Advection (JAS)
25N
20N
15N
10N
5N
EQ
5S
10S
15S
20S
30E
40E
50E
60E
70E
80E
90E
100E
110E
120E
130E
−3
−1
1
3